Materials & Design 234 (2023) 112363

Contents lists available at ScienceDirect

Materials & Design

journal homepage: www.elsevier.com/locate/matdes

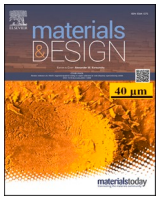

Cracking mechanisms in additively manufactured pure tungsten from printing single tracks, thin walls and cubes

Jinhan Chen [a,b,1], Mingshen Li [a,1], Kailun Li [c], Wenjing Zhang [a,*], Zhengmao Yang [d,*], Congcong Zhao [e], Jing Ma [a], Wei Liu [a,*]

[a] School of Materials Science and Engineering, Tsinghua University, Beijing 100084, China
[b] AVIC Manufacturing Technology Institute, Beijing 100024, China
[c] Institute of Engineering Thermophysics, Chinese Academy of Sciences, Beijing 100190, China
[d] Institute of Mechanics, Chinese Academy of Sciences, Beijing 100190, China
[e] Jihua Laboratory, Foshan 528000, China

ARTICLE INFO

Keywords:
Cracking
Tungsten
Additive manufacturing
Grain boundaries
Microstructures
Geometric effect

ABSTRACT

Cracking is a critical issue in the additive manufacturing of pure tungsten (W). To eliminate crack formation, it is imperative to gain an in-depth understanding of the underlying mechanisms behind this process. In this study, we systematically investigated the crack behaviors of single tracks, thin walls, and cubes fabricated using powder bed fusion–laser beam (PBF–LB) technology with nonrotational parallel-hatching scanning. The energy framework was employed to elucidate the mechanism of crack formation. The longitudinal cracks appearing in the microstructures of single tracks and the through cracks existing in thin walls and cubes were characterized. Notably, periodic through cracks extended upward across the sample, appearing at every single hatch in unidirectional samples and at every other hatch in bidirectional samples. The horizontal, longitudinal, and transverse cross sections of cubes were studied to clarify the correlation between through crack arrangement and solidification microstructure. Based on a comprehensive analysis of grain boundaries, we proposed a deformation-cracking competition mechanism in PBF–LB tungsten. Geometric effects in the crack and microstructure were also revealed. This study could provide valuable insights into the formation of cracks in PBF–LB tungsten and serve as a foundation for future investigations aimed at eliminating cracks.

1. Introduction

Cracking is a critical challenge limiting the production of additively manufactured tungsten (W) as a plasma-facing material in nuclear fusion devices [1–5]. The body-centered cubic (BCC) crystal structure of pure W challenges the initiation of motion within its slip systems due to the limited mobility of dislocations, thereby restricting the number of active independent slip systems [6]. Although previous studies have reported that powder bed fusion–laser beam (PBF–LB) W samples with densities reaching 99 % have been fabricated, intergranular cracks still persist. These cracks severely deteriorate the thermal and mechanical properties of W materials. Efforts have been made to reduce the crack density of PBF–LB W by preheating substrates [7,8], modifying powders [9], introducing secondary phases [10–12] and optimizing processing parameters [13–15]. However, none of these efforts can totally eliminate cracks.

PBF–LB W cracks can be distinguished into longitudinal cracks and transverse cracks, and they can form crack networks in three-dimensional (3D) space [1,8]. The direct external reason for crack formation is the thermal stress, which stems from the high cooling rates and high thermal gradient during the PBF–LB process. Many scholars have investigated thermal stress and residual stress by experiments and simulations involving various techniques, including the hole-drilling method [16], contour method [17], and neutron diffraction method [18]. Generally, when the external stress exceeds the elastic deformation limits of materials, the part undergoes plastic deformation. Due to the high ductile-to-brittle transition temperature (DBTT), it is quite difficult for W to plastically deform during PBF–LB, presenting as a small number of dislocations generated in the microstructure [11]. Thus, the majority of thermal stress is relieved primarily through crack formation rather

* Corresponding authors.
E-mail addresses: wjzhangneu@163.com (W. Zhang), zmyang@imech.ac.cn (Z. Yang), liuw@mail.tsinghua.edu.cn (W. Liu).
[1] Equally contributed.

https://doi.org/10.1016/j.matdes.2023.112363
Received 24 May 2023; Received in revised form 23 September 2023; Accepted 24 September 2023
Available online 26 September 2023

than dislocation motion and plastic deformation, resulting in crack formation in W during PBF–LB. Even preheating at 1000 °C does not completely eliminate cracks in PBF–LB W bulks [19], demonstrating that the thermal stress is too high to eliminate cracks.

According to the abovementioned studies, crack elimination in PBF–LB W is indeed a challenge. To solve this problem, it is believed that a thorough understanding of the crack formation mechanism should be gained first. Several scholars have focused on the crack formation mechanism in PBF–LB W, either focusing on the temporal aspect, i.e., the in situ cracking process, or the spatial aspect, i.e., the postmortem characterization of crack morphology. An excellent in situ high-speed video study from Vrancken et al. [20] revealed the dynamic formation of transverse cracks in single laser-melted tracks and inferred the cracking temperature to range between 450 K and 650 K. However, the researchers minimally reported on the dynamic aspects of longitudinal cracks.

Given the significant influence of microstructure on crack formation, it is imperative to conduct postmortem analyses focusing on the microstructures and morphologies of cracks. In a previous study, Wang et al. [1] performed postmortem characterization of longitudinal cracks and established a correlation between them and laser hatching in the PBF–LB W cube. However, previous experiments involving PBF–LB W predominantly involved scanning strategies incorporating interlayer rotation [8,10,21–23]. Under interlayer rotation conditions, the crack networks within PBF–LB W structures become considerably intricate due to potential coupling and connection between longitudinal and transverse cracks, thereby bringing additional challenges for crack analysis.

To mitigate the aforementioned drawback in crack analysis while taking into account the observation that the longitudinal crack aligns with the central line of the fusion zone (FZ), it is reasonable to propose that parallel-hatching scanning strategies without interlayer rotation, including nonrotating unidirectional or bidirectional scanning strategies, may result in the formation of upward-extending cracks across the sample, i.e., **through cracks**. Specifically, in unidirectional scanning, all scan vectors are oriented in a single direction, whereas in bidirectional scanning, the scan vectors alternate their direction periodically. A previous study involved parallel-hatching strategies to analyze the defect distribution in printed AlSi10Mg [24]. We believe that the implementation of parallel-hatching strategies in PBF–LB for manufacturing W can effectively confine cracks to specific locations within components, thereby providing novel insights into the underlying mechanisms governing crack formation.

In this study, we systematically investigated the crack behaviors of single tracks, thin walls, and cubes in PBF–LB W using nonrotational parallel-hatching scanning strategies. The cracks were characterized and classified, and their underlying mechanisms were discussed. Notably, the through cracks exhibited a periodic arrangement; however, their arrangement varied under different scanning strategies. For instance, in the unidirectional sample, through cracks appeared at every single hatch, whereas in the bidirectional sample, they appeared at every other hatch. Based on an analysis of grain boundaries, we proposed a mechanism involving competition between deformation and cracking in PBF–LB W. Solutions to mitigate cracking during additive manufacturing of W were presented in this study.

2. Methods

2.1. PBF–LB deposition experiments of single tracks, thin walls and cubes

Spherical pure tungsten (purity > 99.95 % and sphericity > 95 %) powders were supplied by Guangdong Yinna Technology Co., Ltd. (Guangdong, China). The average size of the powder was 15 μm, and its oxygen content was as low as 300 ppm. The powders were directly prepared by the electric explosion method of metal wire with the product specification of 5–25 μm, which was beneficial to the PBF–LB process.

The PBF–LB experiments were carried out in an SLM 280 machine (SLM-Solutions Group AG, Germany) composed of a 700-W Yb/YAG fiber continual wave laser with a beam focus diameter of approximately 100 μm. Argon was used as the protective gas, and the oxygen content was controlled below 500 ppm. Substrate preheating was not used in this experiment. Fig. 1 shows a summary of schematic diagrams for scanning strategies of the manufacturing structures. The details were as follows:

In the process of single-track deposition in Fig. 1(a), thin hot-rolled plates of pure tungsten were prepared as substrates to ensure the identity with powders. The laser power (P) was varied from 250 to 400 W in steps of 50 W, and the scanning speed (v) was varied from 100 to 600 mm/s in steps of 100 mm/s. Melting tracks with lengths of 20 mm were processed. Each single track was duplicated three times under the same processing conditions.

In the process of cube deposition in Fig. 1(b_1, b_2), a nonrotational parallel-hatching strategy, including unidirectional and bidirectional, was designed to fabricate the W cubes. A 10-layer thin wall sample consisting of one to ten melt tracks with unidirectional scanning parameters was integrated on a preprinted W cuboid through a unidirectional scanning strategy, as shown in Fig. 1(c). There were several melt track spacings between the thin walls. There was no overlapping misalignment between the thin walls and the preprinted cuboid. The thin walls consisting of different melt tracks would experience different temperature and stress fields during the PBF–LB process, helping to reveal the size effect of the material. In addition, a 10-layer height cube built on a preprinted W cuboid with the same laser parameters was produced. The hatch distance of the two cubes was misaligned by $\Delta h = 50$ μm, as shown in Fig. 1(d). The hatch distance (h_d) and layer thickness (t) values of all cubes were 100 μm and 25 μm, respectively. The oxygen contents of the samples were measured by X-ray fluorescence spectrometry (ARL Perform X, Thermo Fisher, China).

For the ease of follow-up discussions, the plane perpendicular to the building direction (BD) was defined as the horizontal plane, the plane perpendicular to the scanning direction (SD) was defined as the longitudinal plane, and the plane perpendicular to the transverse direction (TD) was defined as the transverse plane. The dimensions of the deposited and preprinted cuboids were both 4 mm (TD) × 3 mm (SD) × 2 mm (BD). The printed plate was allowed to cool before the samples were then printed on top of it. Table 1 presents a summary of the designed strategies for manufacturing single tracks, thin walls and cubes with specific processing parameters.

2.2. Microstructural characterization

For the microstructural analysis, the substrates and fabricated samples were sectioned and mechanically ground with conventional metallographic methods using fixtures. Then, the substrates were polished using an argon ion beam polisher (SM-09010 Cross-section Polisher, JEOL Co., Ltd., Tokyo, Japan). Additionally, fabricated samples were electropolished using a 1.5 wt% NaOH solution at a voltage of 9.8 V for 90 s at room temperature to clearly reveal the cracks.

The images of scanning tracks on the top surface were characterized by optical microscopy (OM; Scope A1, ZEISS, Germany). The morphologies of melting pools were determined by scanning electron microscopy (SEM; TESCAN MIRA 3LMH, Bron, Czech Republic) equipped with secondary electron (SE), back-scattered electron (BSE) and electron backscattered diffraction (EBSD) detectors on an HKL Nordlys orientation imaging microstructure system (Oxford Instruments, Oxford, UK). The EBSD data were analyzed using HKL channel 5 software packages. The average sizes of the grains were measured using the area method without deviation as prescribed according to ASTM E112 by HKL channel 5 software packages. In this study, all inverse pole figure (IPF) mappings were analyzed along the z direction. The surface molten pool and fracture characteristics of the samples were examined using laser

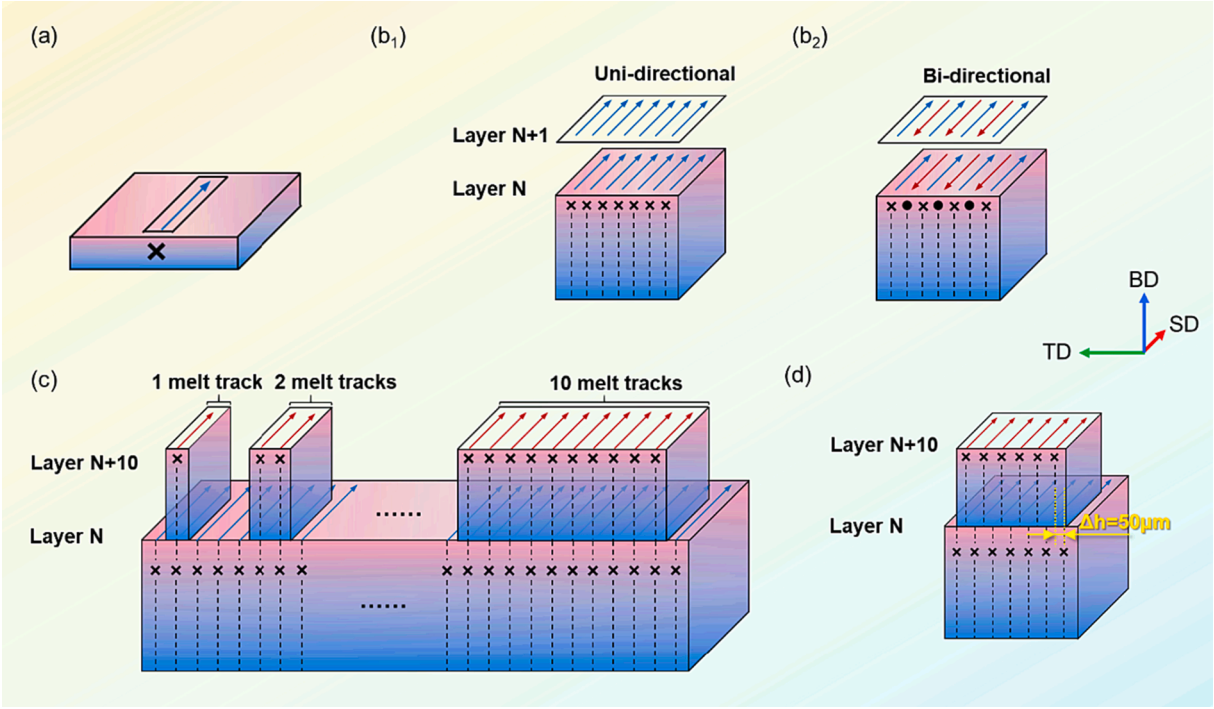

Fig. 1. Summary of schematic diagrams for scanning strategies of the manufacturing of single tracks, thin walls and cubes. (a) Single-track deposition on a W substrate. Interlayer nonrotating (b_1) unidirectional and (b_2) bidirectional scanning strategies of deposited cubes. (c) 10-layer thin wall sample consisted of one to ten melt tracks integrated on a printed W cubic base plate. (d) 10-layer height cube built on a preprinted W base plate with a misaligned hatch distance of $\Delta h = 50$ μm.

Table 1
Designed strategies for manufacturing single tracks, thin walls and cubes with different processing parameters in detail.

	Single tracks	Cubes		Thin walls	Cubes
Memo	Printed on the hot-rolled plate	Different scanning strategy		One to ten melt tracks integrated on a preprinted cuboid	Printed on a preprinted cuboid with $\Delta h = 50$ μm
P (W)	250–400	300	300	300	300
v (mm/s)	100–600	400	400	400	400
t (μm)	~25	25	25	25	25
h_d (μm)	–	100	100	100	100
Interlayer rotation	–	0	0	0	0
Scanning direction	–	**uni-**	**bi-**	uni-	uni-
Schematic diagram	Fig. 1(a)	Fig. 1 (b_1)	Fig. 1 (b_2)	Fig. 1(c)	Fig. 1(d)

confocal scanning microscopy (LCSM; ZEISS LSM 900, Germany).

2.3. Finite element model of the PBF–LB process

To obtain quantitative thermal stress data within the melting pool, a finite element (FE) simulation was carried out using Ansys software. As shown in Fig. 2, the dimensions of the substrate in the FE model were 4 × 0.5 × 1 mm. Simulations were conducted over half of the geometry, taking advantage of symmetry. By considering the calculation efficiency and computational precision, the substrate was finely meshed adjacent to the laser irradiating area and was coarsen meshed away from the laser irradiating area. The layer thicknesses of single-track powder beds were approximately 25 μm. The widths of single tracks corresponded to their actual width measured in the experiments under different process parameters. The temperature-dependent thermal-physical parameters of tungsten are shown in Table 2.

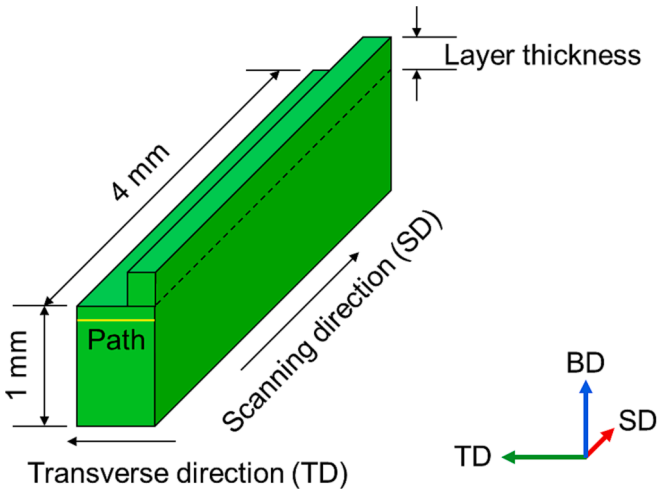

Fig. 2. Solution domain for the heat transfer and mechanical analysis.

Part of the heat dissipated through convection and radiation, and the remaining heat was conducted to the substrate. The spatiotemporal distribution of the temperature field satisfied the Fourier heat conduction equation [27,28]:

$$\rho c(T)\frac{\partial T}{\partial t} = \frac{\partial}{\partial x}\left(k\frac{\partial T}{\partial x}\right) + \frac{\partial}{\partial y}\left(k\frac{\partial T}{\partial y}\right) + \frac{\partial}{\partial z}\left(k\frac{\partial T}{\partial z}\right) + Q \quad (1)$$

where ρ is the density of the material (19.35 g/cm^3), c is the heat specific capacity, T is the temperature of the powder bed, k is the thermal conductivity, and Q is the volumetric heat generation.

- Initial conditions

$$T(x, y, z, t)|_{t=0} = T_0(x, y, z) \in D \quad (2)$$

where D is the scanned region and T_0 is the initial temperature when

Table 2
Temperature-dependent parameters for the FE simulation of pure W [25,26].

Temperature (K)	Young's modulus (GPa)	Temperature (K)	Linear expansion coefficient (/K)	Temperature (K)	Yield stress (MPa)	Temperature (K)	Heat specific capacity (J/(g·K))	Temperature (K)	Thermal conductivity (W/(m·K))
273	410	300	4.49E−6	273	1600	300	130	300	174
573	399	600	4.75E−6	573	1090	500	137	500	146
873	387	1000	5.02E−6	873	732	1000	145	1000	118
1173	373	1400	5.46E−6	1173	550	1500	153	1500	108
1473	358	1800	6.11E−6	1473	200	2000	162	2000	99
1773	341	2200	6.89E−6	1773	82	2500	172	2500	91
2073	323	2600	7.76E−6	2073	63	3000	195	3000	85
2373	304	3000	9.05E−6	2373	31	3500	228	3500	80
2673	283	3400	1.16E−5			3600	239	3600	79
2973	261								
3273	238								
3573	213								

time t = 0 and is taken as 22 °C.

• Boundary conditions

$$k\frac{\partial T}{\partial n} - q + h_c(T - T_0) + X\varepsilon\left(T^4 - T_0^4\right) = 0(x, y, z) \in S \tag{3}$$

where S is the surface, n is the normal vector of surface S, ε is the emissivity (0.35), h_c is the heat convection coefficient ($20\,W/(m^2 \bullet K)$), X is the Stefan–Boltzmann constant ($5.67 \times 10^{-8}\,W/(m^2 \bullet K^4)$) and q is the input heat flux.

The Goldak double ellipsoid heat source model was used as the heat load, which could obtain reasonable results in this simulation. The laser intensity distribution conformed to a relationship, which was expressed as follows:

$$Q_r = \frac{6\sqrt{3}QAf_r}{\pi\sqrt{\pi}a_r bc}\exp\left[-3\left(\frac{x^2}{a_r^2} + \frac{y^2}{b^2} + \frac{z^2}{c^2}\right)\right] \tag{4}$$

$$Q_b = \frac{6\sqrt{3}QAf_b}{\pi\sqrt{\pi}a_b bc}\exp\left[-3\left(\frac{x^2}{a_b^2} + \frac{y^2}{b^2} + \frac{z^2}{c^2}\right)\right] \tag{5}$$

where Q is the total input heat flux, Q_r and Q_b are the energy distributions at two points in the double ellipsoid, A is the absorptivity of the powder material (0.68), a, b, and c are the three-axis shaft lengths, x, y and z are the distances from one point in the irradiation area to the central position of the laser beam, and f is the energy distribution coefficient in front of and behind the double ellipsoid, $f_r + f_b = 2$.

The thermal stress calculation is based on the Ansys transient stress analysis using the temperature calculation results as loading. The principle of the FE analysis model for stress and strain calculations could be interpreted as the finite element solution of static force equilibrium equations in the discretized solution domain for the temperature data calculated using the heat transfer and fluid flow model. The stresses along the × and y directions were described as the longitudinal and transverse stresses, respectively. From the calculated stress field, the individual residual stress component was extracted along the path, as shown in Fig. 2.

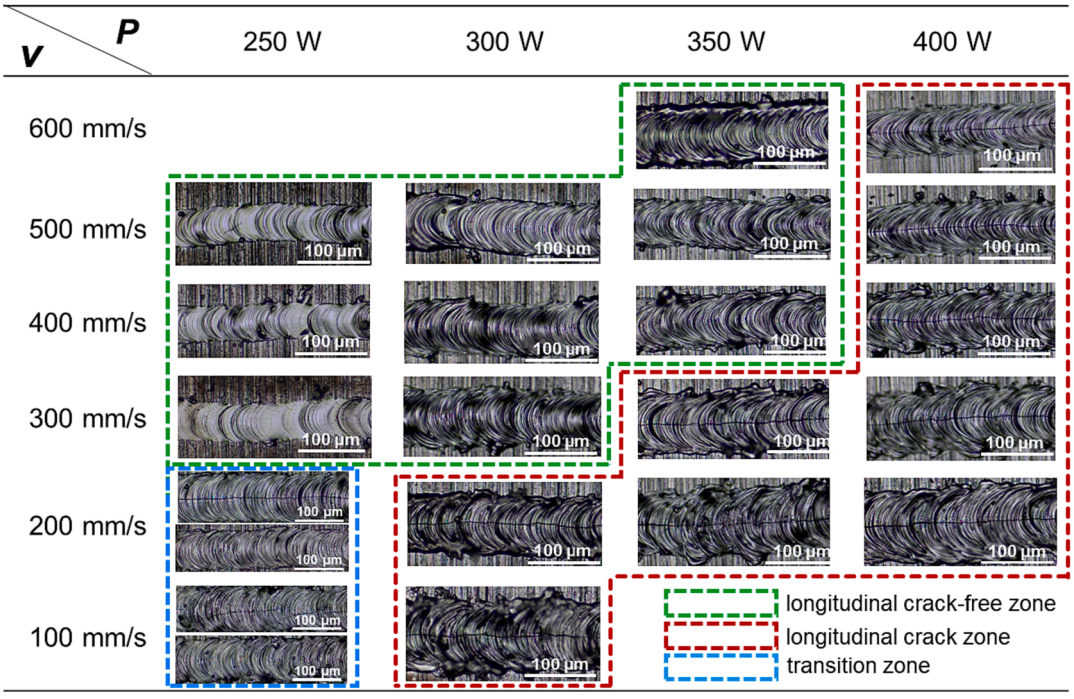

Fig. 3. Process map showing morphologies of longitudinal cracking with different scanning parameters. Three sides separated by dashed polygons of green, red and blue represent the longitudinal crack-free zone, longitudinal crack zone and transition zone, respectively.

3. Results

3.1. Crack morphologies and solidification microstructures in PBF–LB W single tracks

To analyze the overall cracking behaviors of single tracks in W under different energy inputs, single-track experiments were conducted using different linear energy densities (LEDs), defined as P/v.

Fig. 3 shows a process map relating single track morphologies to different sets of parameters. Three zones can be distinguished. In the lower-right corner with a high LED, i.e., in the red dashed region in Fig. 3, one pronounced long straight crack along the SD throughout the center of each single track is revealed. On the upper-left corner with a low LED, i.e., in the green dashed region in Fig. 3, cracks along the SD of single tracks are absent. In the transition region of the LED ranges, not all single track experiments develop longitudinal cracks, as represented by the blue dashed region in Fig. 3. The process map clearly demonstrates the presence of critical processing parameters that significantly influence the occurrence of long straight cracks throughout the center of single tracks. When P exceeds 400 W, crack sensitivity is greatly enhanced.

In particular, in the magnified longitudinal crack zone, the longitudinal cracks and branching cracks spread radially at the middle of the single track, as shown in Fig. 4(a). In the enlarged images in Fig. 4(b), the contrasting characteristics of the grain morphology can be clearly seen. The presence of narrow cracks, which have been observed to aggregate at the grain boundaries (GBs), is revealed.

To investigate the correlation between the cracking behavior and microstructure, SEM and the corresponding EBSD images of longitudinal cross-sections of single tracks are examined and displayed in Fig. 5(a), with different scanning speeds at fixed P = 350 W. With decreasing scanning speed v, the depth, width, and depth-to-width aspect ratio of the molten pool increase, and the susceptibility to cracking in the center region of the fusion zone increases. When v is lower than 300 mm/s, the generation of a longitudinal crack extending from the bottom to the top surface of the FZ can be observed. Cracks are initiated and propagated in the heat-affected zone adjacent to the FZ. IPF maps reveal two regions regardless of the FZ sizes: the columnar grains perpendicular to the FZ boundary and the equiaxed grains in the FZ center.

The growth directions of the columnar grains adjacent to the fusion boundary are mostly perpendicular to the fusion line in the longitudinal plane since the local maximum heat flow directions are perpendicular to the fusion boundary [29]. The average size of the equiaxed grains in close proximity to the FZ center is quantified from the bottom to the top surfaces. Notably, the equiaxed grains located in the FZ center should be the short-axis projection of the 3D columnar grains [29]. The investigation reveals that irrespective of the FZ size, the equiaxed grain sizes range from 5 to 6.5 μm, exhibiting similar grain dimensions across varying scanning speeds. Although the decreasing scanning speed v does not exhibit a prominent increasing trend of the grain size adjacent to the middle of the FZ, it results in a deepening molten pool, which can potentially account for the observed variations in crack behavior. The morphologies, dimensions and distributions of grains in the FZ with different energy densities can be effectively compared based on the findings in Fig. 5. The findings indicate a positive correlation between a relatively large FZ and the occurrence of longitudinal cracks.

3.2. Crack morphologies and solidification microstructures in PBF–LB W cubes

The conducted PBF–LB single track experiments displayed in Section 3.1 have demonstrated the formation of longitudinal cracks extending from the bottom to the top surface of the molten pool, precisely positioned at the middle of the fusion zone. However, PBF–LB technology employs a track-by-track stacking process for materials from one dimension (1D) to three dimensions, resulting in the generation of a distinct periodic microstructure and morphology. Therefore, it is evident that the utilization of a nonrotating unidirectional or bidirectional strategy in the construction of 3D stacking cubes inevitably leads to the formation of **through cracks**, which are extended along the stacked FZ midline from the sample root to the top. To validate the progression of single tracked cracks in 3D components, a structural cube experiment can be designed with nonrotational scanning between adjacent layers to mitigate the influences of interlayer rotational variables on crack formation. First, based on the results of single tracks in Fig. 5(a), unidirectional cubes were fabricated with a scanning speed of 200 to 600 mm/s (in increments of 100 mm/s) at P = 350 W to investigate the influences of different energy densities on crack formation, as depicted in Fig. 5(b). Through cracks and transversely extended cracks can be observed in all printed parameters. Moreover, a significant increase in the crack density of cubes is observed at P = 350 W and v = 200 mm/s.

Fig. 6 provides an overview of the crack morphologies and grain structures in the W cube fabricated using unidirectional and bidirectional scanning strategies, employing pseudo-three-dimensional photographs that integrate SEM maps and EBSD maps in horizontal, longitudinal, transverse and diagonal orientations. Specifically, the transverse planes depicted in Fig. 6(a_1, b_1) represent fracture surfaces, whereas the remaining planes correspond to polished surfaces. The methodology employed for generating the fracture surface will be further elucidated in Section 3.2.2.

The most intriguing feature depicted in Fig. 6 is the long straight crack in the longitudinal plane and horizontal plane, extending upward across the whole sample. This crack is defined as a through crack. The unexpected aspect lies in the arrangement observed within these

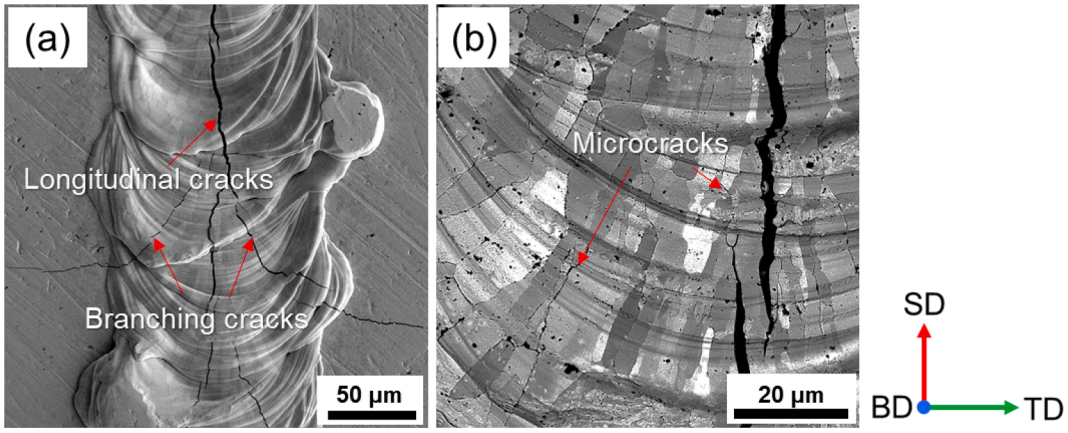

Fig. 4. Top morphologies of cracks at the middle of the single track with v = 300 mm/s at P = 350 W.

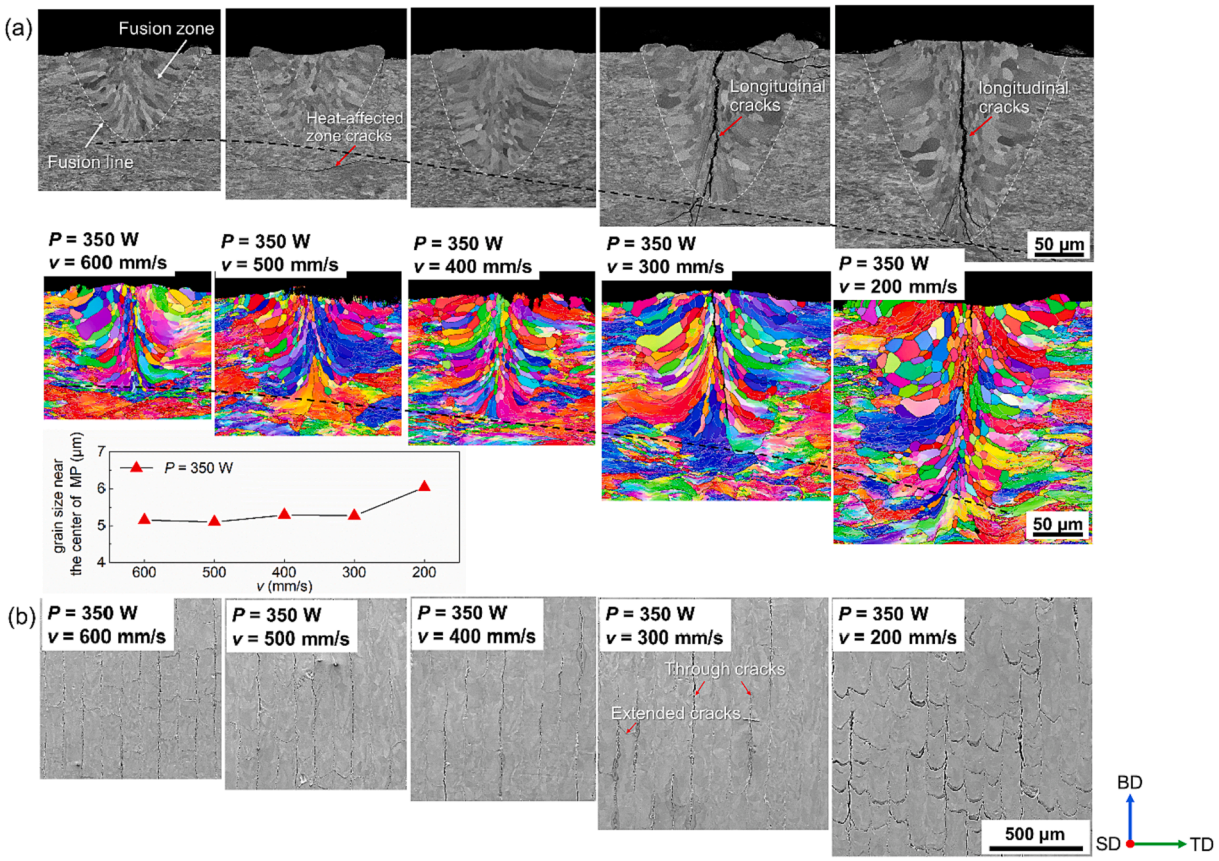

Fig. 5. (a) SEM and EBSD images of the cross-section longitudinal plane of single tracks with 200–600 mm/s scanning speeds at P = 350 W, with the five images corresponding to Fig. 3. The black dashed lines represent the variable molten pool depth. An image of the average sizes of grains close to the middle of the fusion zone from the bottom to the top surfaces of the molten pool is shown. (b) Crack arrangements of PBF–LB pure W cubes under P = 350 W with 200–600 mm/s scanning speeds.

through cracks, which reveals distinct structural characteristics under the two parallel-hatching scanning strategies, i.e., through cracks appear at every single hatch in the unidirectional sample and at every other hatch in the bidirectional sample. The widths of through cracks in the bidirectional sample are more pronounced than those in the unidirectional sample. In fact, through cracks have been reported in studies by Wang [1] and Todo [30], but limited attention has been given to the arrangement of periodically distributed materials through cracks.

The next three sections will feature discussions of the microstructures and crack morphologies in these planes separately.

3.2.1. *Crack arrangements and grain structures in longitudinal planes*

Fig. 7 shows a comparison of the grain structure and crack arrangement in the longitudinal planes with unidirectional and bidirectional scanning strategies. The microstructure in a unidirectional manner exhibits a ladder-like arrangement, where rectangular grains adjacent to each other are confined between two neighboring scan vectors. The bidirectional microstructure exhibits a curved, epitaxial columnar grain structure with an extremely large aspect ratio, spanning hundreds of microns. The unidirectional microstructure exhibits a crack arrangement characterized by periodic through cracks positioned at the middle of the fusion zone at every single hatch and by extended cracks branching along the Y-direction curved grain boundaries (Fig. 7(b_1)); the bidirectional microstructure predominantly exhibits periodically arranged through cracks at every other hatch. The average widths of the through cracks under the unidirectional and bidirectional scanning strategies are approximately 1.4 μm and 3.6 μm, respectively.

The high magnification in Fig. 8 reveals the distributions and morphologies of cracks in the PBF–LB W cube. In addition to through cracks (Fig. 7(b_1, b_2) and Fig. 8(a)), transversely extended cracks (Fig. 8((b_1, b_2)), nonextended cracks (Fig. 8(d, e)) and nanopores (Fig. 8(c_2)) can be observed. The morphologies, scales and locations of defects are summarized as follows:

(i) Through cracks (TCs), which are long and straight intergranular cracks formed at the FZ center under specific conditions with a nonrotational scanning strategy between adjacent layers in the 3D parts. The periodic distributions of these structures are based on hatch spacing, serving as the fundamental unit, and they exhibit lengths ranging from hundreds of microns to several millimeters, with widths spanning several microns.
(ii) Transversely extended cracks (ECs), which are intergranular cracks distributed widely in the matrix and aligned with the TD. TCs can be interconnected by ECs. The lengths of the ECs range from several microns to hundreds of microns.
(iii) Nonextended cracks (NECs). NECs are typically distributed randomly throughout the matrix, with a localized concentration observed at a specific section of the grain boundary between two adjacent grains.
(iv) Nanopores. The size of nanopores is on the nanometer scale. The aggregation of these nanopores along grain boundaries is commonly accompanied by the formation of cracks (Fig. 8(d–f)), suggesting their roles as potential nucleation sites for crack initiation. The presence of nanopores has been documented in previous investigations [11,23].

The characteristics of various cracks and nanopores in longitudinal planes are comprehensively summarized, especially the TCs.

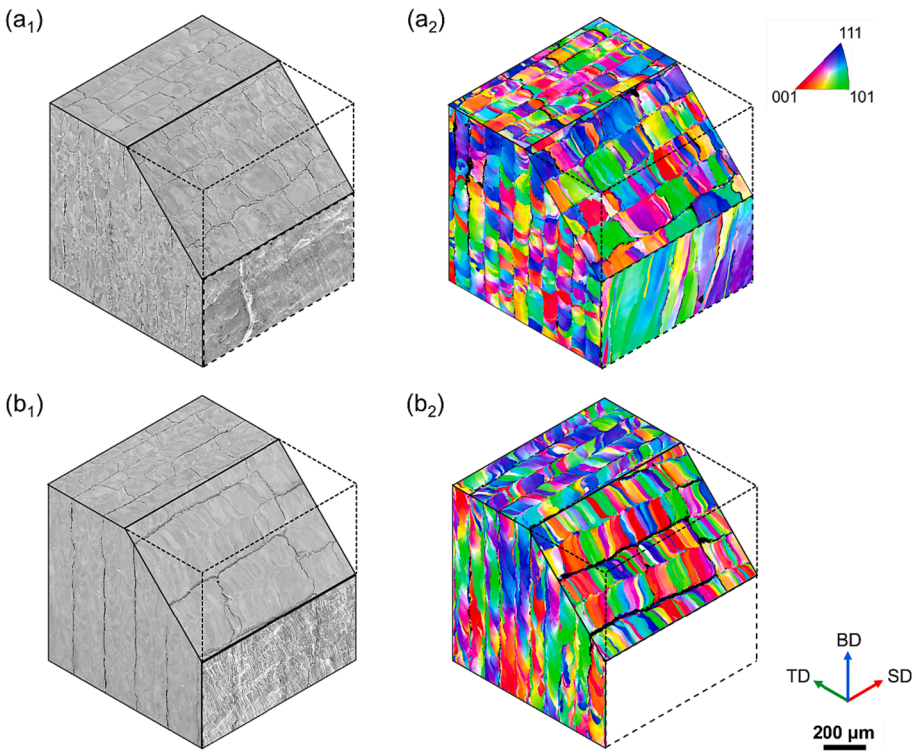

Fig. 6. (a_1, b_1) SEM and (a_2, b_2) EBSD images obtained for three different faces of a cubic sample under (a_1, a_2) unidirectional and (b_1, b_2) bidirectional strategies with P = 300 W and v = 400 mm/s.

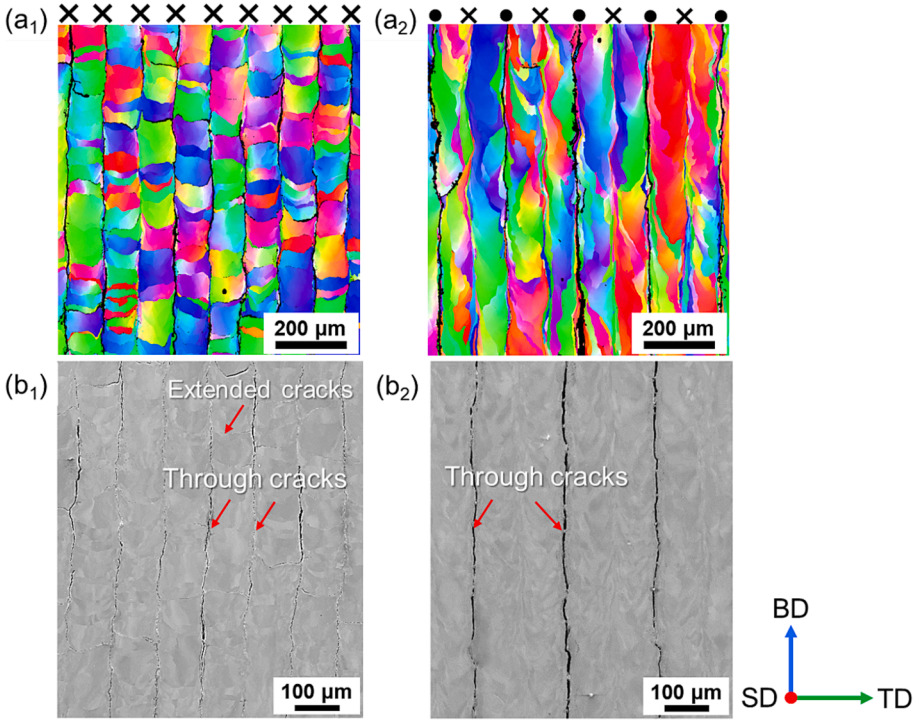

Fig. 7. Comparisons of the grain structures and crack distributions in longitudinal planes with (a_1, b_1) unidirectional and (a_2, b_2) bidirectional strategies extracted from Fig. 6.

Subsequently, the microstructures in the horizontal and transverse planes are presented to facilitate a comprehensive understanding of the TCs.

3.2.2. Crack arrangement and grain structure in horizontal planes

The periodicity of grain morphology can be manifested through the periodicity in the scanning strategy. Fig. 9 presents an illustration of a comparison between surface morphology and grain structure in horizontal planes using two parallel-hatching strategies. Overall, the

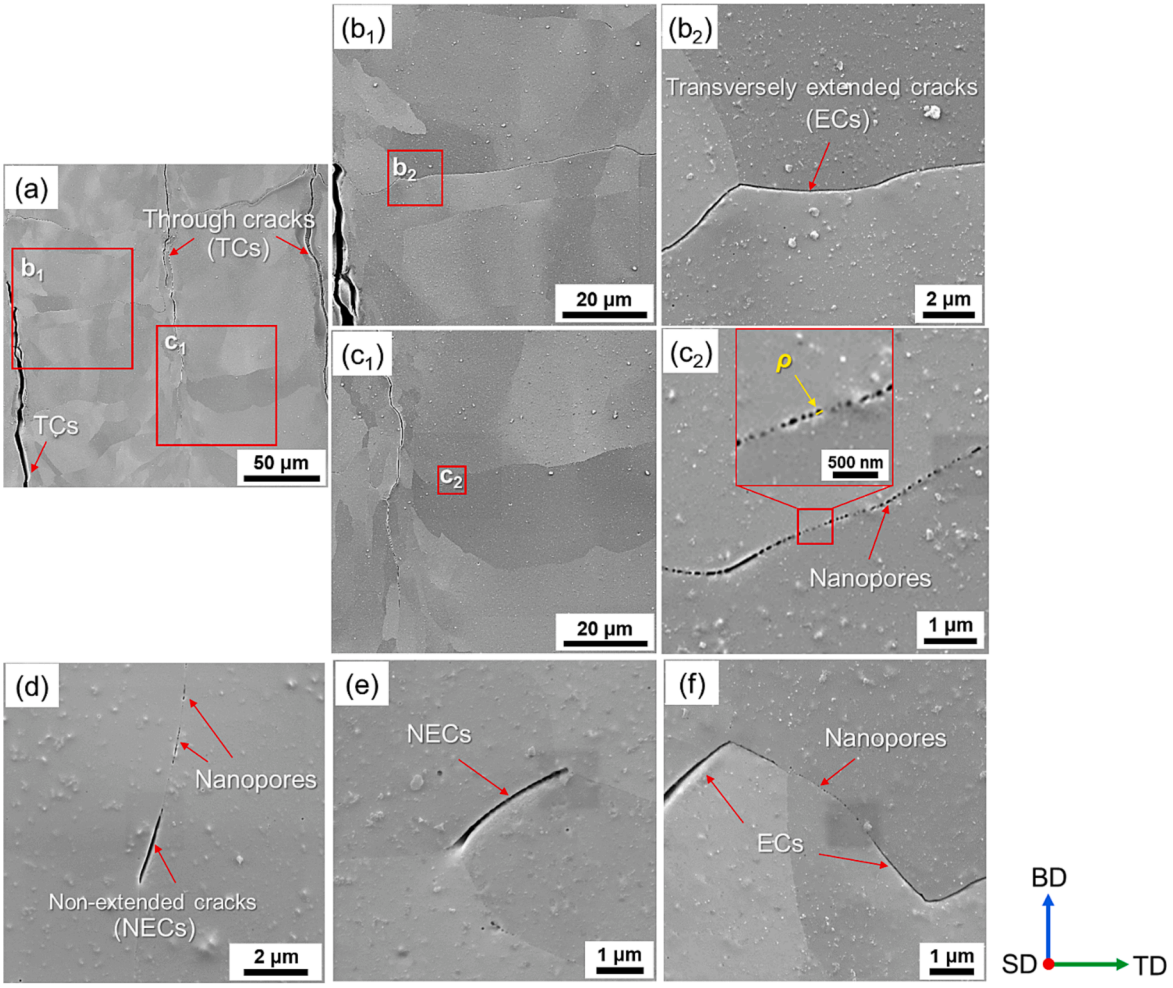

Fig. 8. Distributions and morphologies of cracks and nanopores at high magnification in PBF–LB W cubes with P = 300 W and v = 400 mm/s.

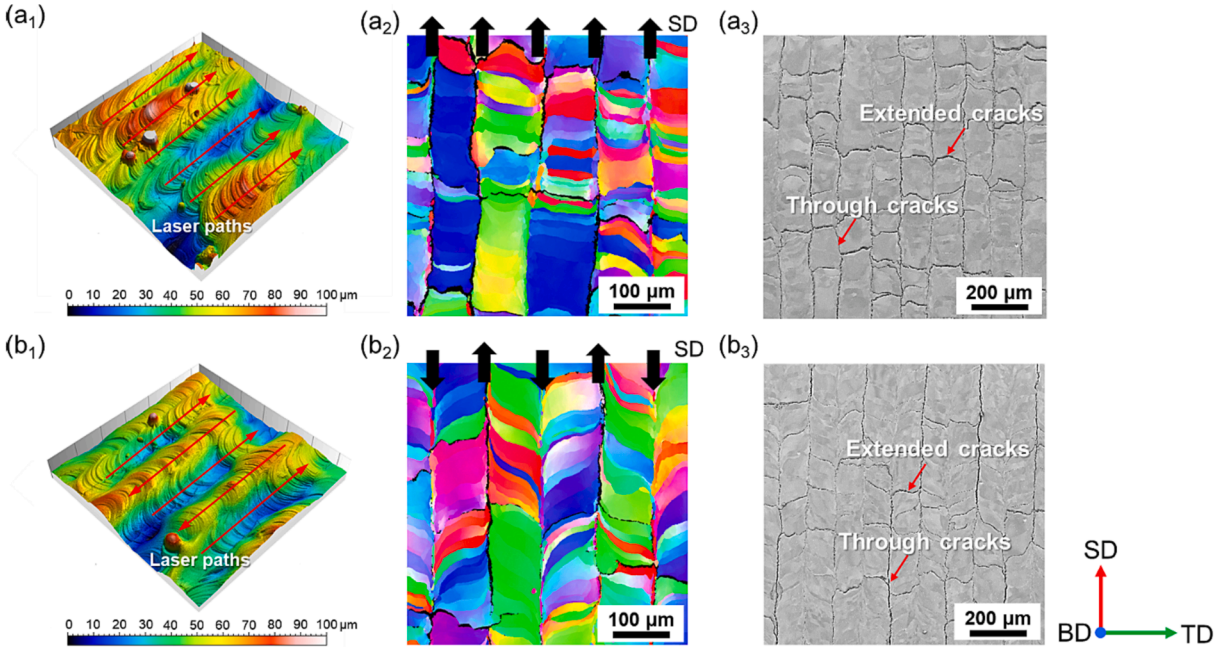

Fig. 9. Surface morphologies and grain structures in the horizontal planes with the two parallel-hatching strategies extracted from Fig. 6. The LCSM images show the topologies of the top surfaces of cubes with (a_1) unidirectional and (b_1) bidirectional strategies. (a_2, b_2) represent the grain structure in horizontal planes with unidirectional and bidirectional strategies, respectively. (a_3, b_3) show the crack morphologies with unidirectional and bidirectional strategies, respectively.

findings in horizontal planes align with those observed in longitudinal planes. The laser confocal scanning microscopy images depicted in Fig. 9 (a_1, b_1) exhibit the surface topographies of the scan tracks corresponding to the employed scanning strategies. The red arrows superimposed on the images indicate the laser scanning directions, effectively highlighting the shape and size of the melt track. It is evident that these melt tracks are distributed periodically, with hatch spacing serving as their fundamental unit.

The EBSD map in Fig. 9(a_2, b_2) reveals that both scanning strategies exhibit characteristic grain structures curving along the scanning direction. However, it should be noted that the grains formed by the unidirectional scanning strategy exhibit a consistent curvature in the same direction, resulting in periodic curved grain structures (Fig. 9(a_2)). Conversely, employing a bidirectional scanning approach leads to an opposite curving direction in adjacent melt tracks, leading to a leaf-shaped periodic grain structure that corresponds to the movement of the laser (Fig. 9(b_2)). The reason for this phenomenon is that the grains tend to align parallel to the direction of the highest thermal gradient, which coincides with the scanning direction. At the convergence point (located at the center of the fusion zone), a small quantity of fine grains is observed, indicating a concentration of grain boundaries in this region. Regarding crack behaviors, we can observe through cracks and transversely extended cracks propagating along the midline of the FZ and at the boundary of curved grains, respectively (Fig. 9(a_3, b_3)). Although bidirectional scanning reveals an arrangement resembling crack appearance at every other hatch in the longitudinal section, it is important to note that the true three-dimensional arrangement may not strictly adhere to this rule, which will be further discussed in Section 4.3.

3.2.3. *Crack arrangements and grain structures in transverse planes*

To facilitate comprehension of the arrangement of through cracks, fracture surfaces were obtained by applying stress in the transverse direction. It is worth noting that due to their inherent weakness, the samples can be easily fractured along these through cracks (Fig. 10(a)). Consequently, the fracture surface coincides with the surface of the through crack. Fig. 10 presents the fracture surfaces observed in both scanning strategies within the transverse plane.

The unidirectional strategy leads to morphologies of the intergranular fracture surface in conjunction with the adjacent layer fracture surfaces, as depicted in Fig. 10(b). Furthermore, the coincidence of the fracture surface and through crack surface allows for the observation of the grain shape within the fusion zone central region, which exhibits an inclination toward the scanning direction. The ground and polished transverse section in Fig. 10(c) reveals the presence of a prominent longitudinal crack along the building direction, which corresponds to the cross-section of the transversely extended cracks described in Section 3.2.2. This observation provides evidence for the interconnectedness of these cracks in three-dimensional space, thereby forming intricate networks. The EBSD map in Fig. 10(d) reveals that columnar grains exhibit a preferential growth direction at approximately 65° to the scanning direction, attributed to epitaxial grain growth influenced by the elliptical pool shape and heat flow orientation. The inclined grain morphology observed in the EBSD map (Fig. 10(d)) corresponds well with the inclined pattern observed on the fracture surface (Fig. 10(b)).

The inclined intergranular fracture morphologies in the bidirectional strategy exhibit similarities to the unidirectional fracture surface. Interestingly, a distinct step feature is clearly observed, where the right

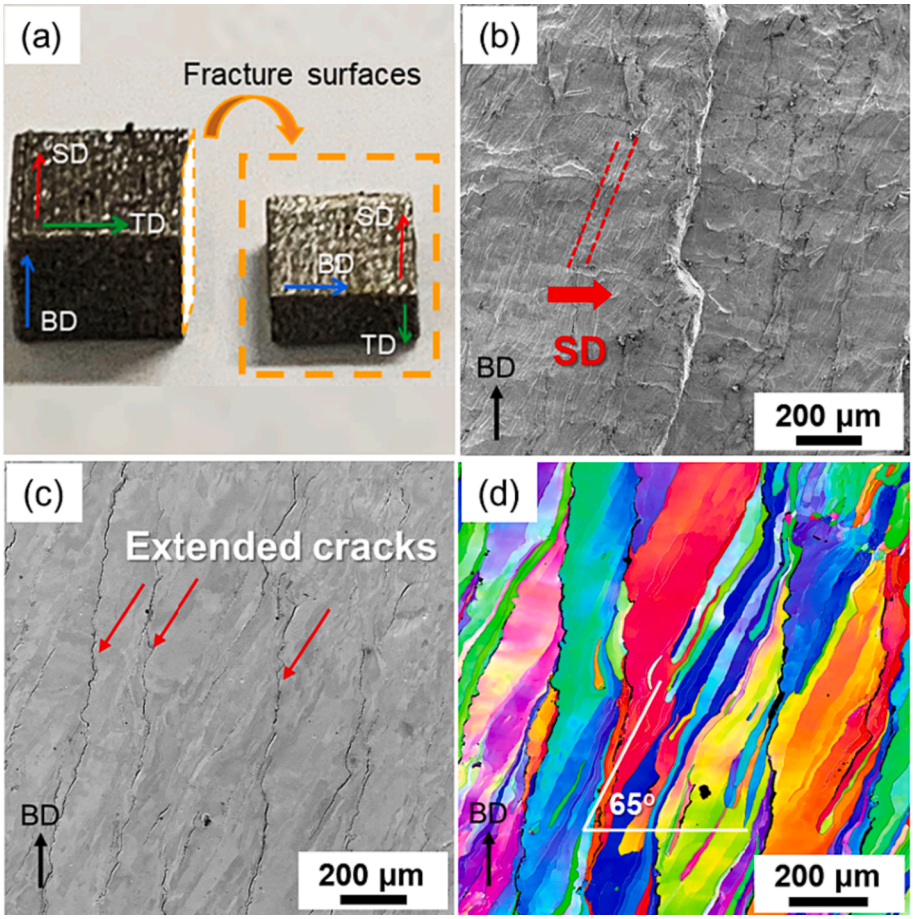

Fig. 10. (a) Optical image of as-built PBF–LB W cubes marked by orange arrows, showing fracture surfaces and grain structures in transverse planes with (b–d) unidirectional and (e–h) bidirectional strategies. (b) The intergranular fracture morphologies with the two-layer fracture surfaces. (c) SEM and (d) EBSD images of the polished microstructure.

side of the step appears higher than the left side (Fig. 11(a)). Fig. 11(b) presents a magnified image selected from Fig. 11(a).

For the bidirectional strategy, the inclined intergranular fracture morphologies are similar to the unidirectional fracture surface. Interestingly, a step where the right side of the step is higher than the left side is clearly observed, as shown in Fig. 11(a). Fig. 11(b) shows the magnified image selected in Fig. 11(a). The pattern on the right side of the step exhibits a rightward inclination, while on the left side, it shows a leftward inclination. The direction of inclination is indicated by the straight dashed line in Fig. 11(b). The fracture topology of Fig. 11(b) is further revealed by the LCSM image in Fig. 11(c). Additionally, the LCSM image confirms a thickness difference of approximately 100 μm for the step, which corresponds to the hatch spacing. Consequently, the relationship between the scanning direction and the grain growth direction can be established. By taking the model of a bidirectional scanning strategy as an example (Fig. 11(d)), epitaxial grain growth occurs from the edge of the molten pool in alignment with the laser scanning direction due to the influence of heat flow.

3.2.4. Through crack propagation in PBF–LB W cubes

According to the aforementioned analysis, periodic through cracks in PBF–LB W cubes propagate along the center of the FZ. To further investigate the stability of through crack propagation, a 10-layer height cube was fabricated on a preprinted base plate with a misalignment of $\Delta h = 50$ μm using a nonrotating unidirectional strategy. The crack morphology and grain structure in the longitudinal plane containing a transition region where the melt tracks are misaligned are depicted in Fig. 12. It is evident that above the transition region, through cracks continue to propagate along the FZ center. The transition region facilitates a deflection of through cracks between the misaligned melt tracks. In the corresponding EBSD analysis (Fig. 12(b, c)), a misaligned ladder-like microstructure is consistently achieved at the transition region. The obtained results demonstrate the formation of through cracks at the FZ center in a stable and reproducible manner, thereby exemplifying the principle of minimum energy.

3.3. Crack arrangement and grain structure in thin wall structures of PBF–LB W

To further investigate the formation of through cracks, a thin-walled sample was designed and printed on a preprinted cubic base plate with identical scanning parameters, comprising one to ten melt tracks. The printing process followed a unidirectional scanning strategy. The arrangement of cracks and microstructures in thin walls consisting of one to ten melt tracks with heights of 10 layers are depicted in Fig. 13. In the preprinted base plate, TCs can be observed at every single hatch, which aligns with the findings presented in Fig. 7(a_1, b_1). The presence of TCs in thin walls was investigated, as shown in Fig. 13(a). No TCs can be observed in thin walls with one or two melt tracks, whereas a continuous extension of TCs from the base plate can be observed in thin walls with more than three melt tracks (indicated by red arrows), suggesting the existence of a size effect and a threshold for through crack formation. The thermal stress is widely acknowledged to be caused by the constraint imposed by the preprinted layers and tracks [31]. Therefore, the observed threshold indicates that both the constraint and thermal stress increase with increasing sample size. Furthermore, the resemblance in microstructure and crack arrangement among thin walls containing more than three tracks suggests that a plateau has been reached in terms of thermal stress.

The EBSD images of the grain structure corresponding to Fig. 13(a) are presented in Fig. 13(b). Epitaxially grown grains along the building direction can be observed in all thin wall samples. In the case of a single track thin wall, columnar grains epitaxially grow from the wall territory toward the center. For thin walls with more than two melt tracks, a ladder-like microstructure similar to that shown in Fig. 7(a1) is observed. In the case of a thin wall with two melt tracks, the grain size is

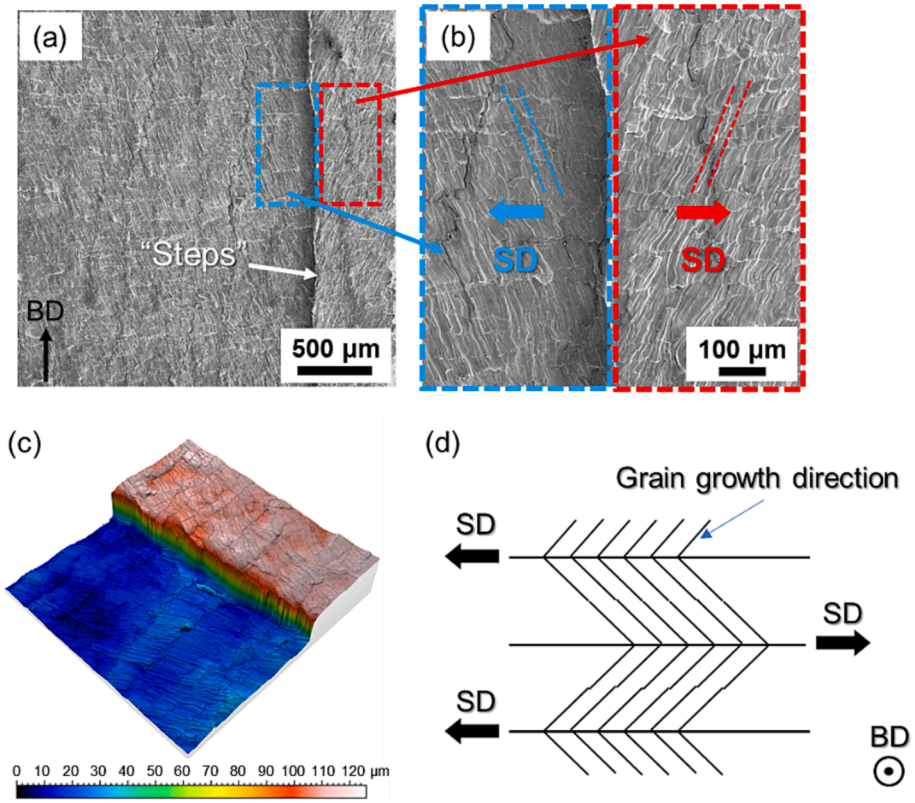

Fig. 11. (a) Intergranular fracture morphologies inclined symmetrically along the BD on the two adjacent layer fracture surfaces. (b) Partially magnified image of (a). (c) LCSM image showing the fracture topology of (b). (d) Schematic illustration of the scanning direction and grain growth during the PBF–LB process of W cubes.

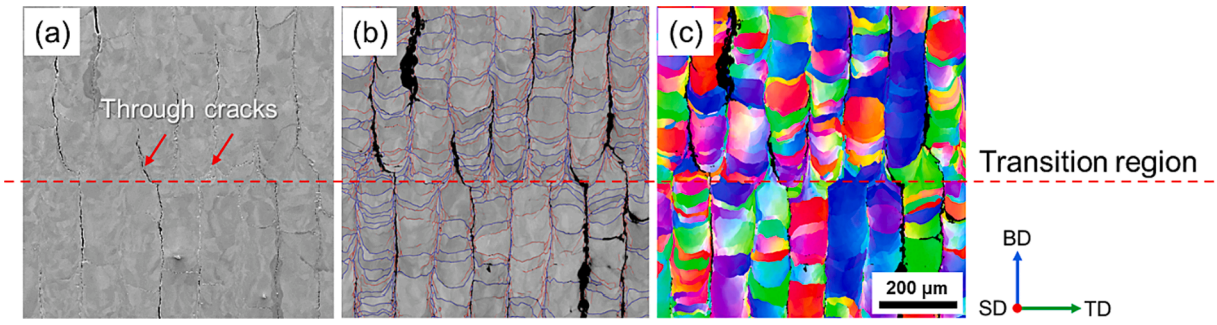

Fig. 12. Crack morphologies and grain structures in the polished longitudinal plane containing transition regions with Δh = 50 μm misaligned melt tracks. (a) SEM image. (b) Corresponding EBSD quality image superimposed HAGBs by blue lines and LAGBs by red lines. (c) Corresponding IPF image.

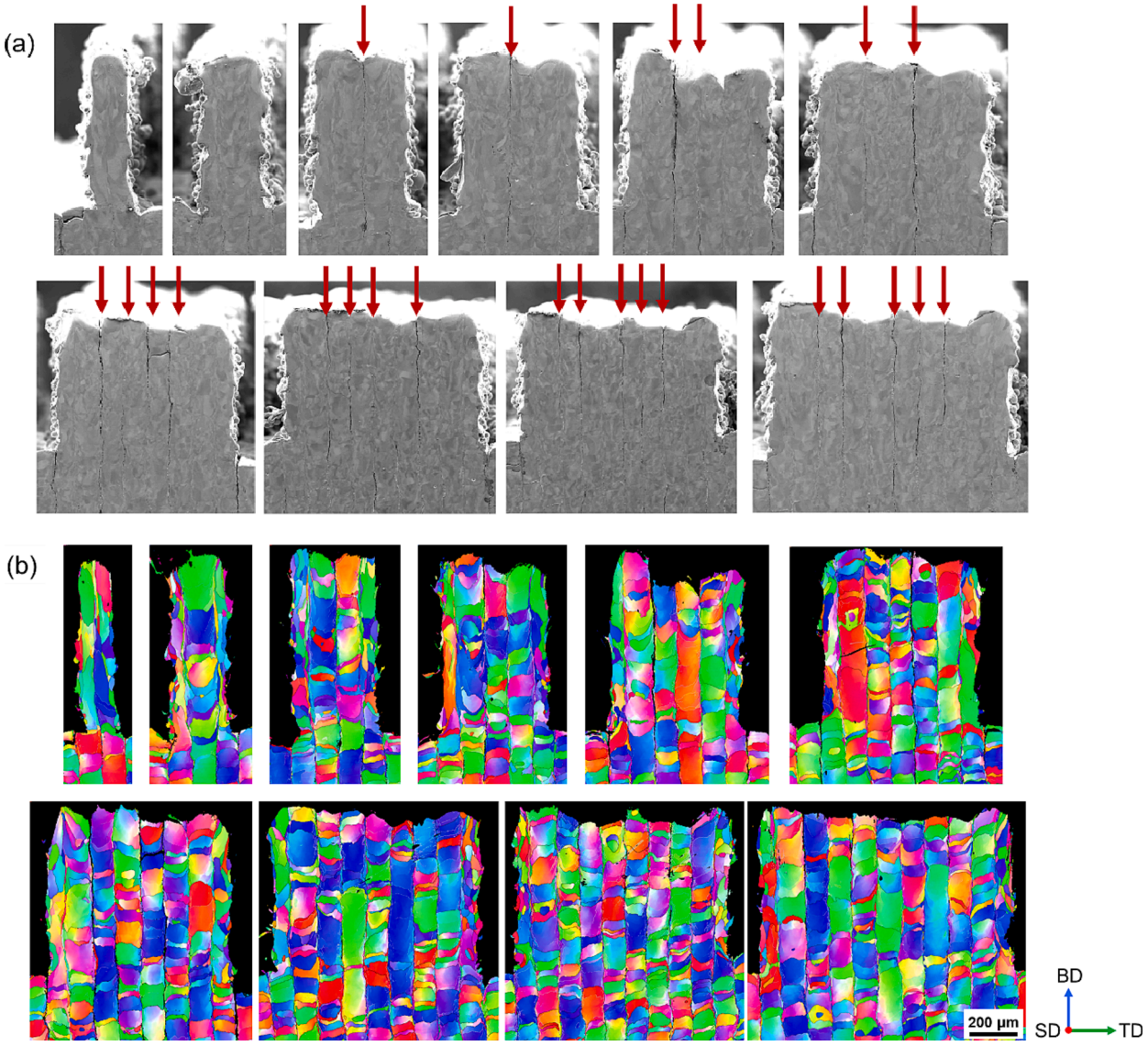

Fig. 13. (a) SEM and (b) the corresponding IPF images showing the cracks and microstructures of the thin wall sample consisting of one to ten melt tracks with 10-layer heights. The red arrows indicate the generation location of TCs, and the white dashed lines represent the centerline of the fusion zone.

slightly larger than that of the base plate, whereas in thin walls with more than three melt tracks, the grain size remains consistent with that of the base plate. This observation implies that for thin walls with multiple melt tracks (typically exceeding three), the level of heat dissipation is nearly equivalent to that of the preprinted base plate, except for the first and last melt tracks. Therefore, it can be inferred that the reduction in wall thickness (i.e., minimizing scan tracks) leads to an increase in solidification microstructure, which is primarily attributed to alterations in the thermal field. The thermal history of multitrack thin walls exhibits similarities with a cube, thus offering valuable insights

into crack formation, which will be further elaborated upon in Section 4.4.

4. Discussion

To elucidate the microstructure and distribution of cracks relative to the various sample shapes mentioned in Section 3, namely, single tracks, thin walls, and cubes, we present an explanatory framework based on microstructural analysis and energy assessment. For enhanced clarity, longitudinal cracks are exclusively discussed during the analysis of single tracks, while through cracks are only addressed when analyzing thin walls and cubes.

4.1. Nanopore weakening effect in PBF–LB W

During the PBF–LB process, a steep temperature gradient induces significant thermal stress, resulting in substantial strain energy accumulation. Within an energetic framework, crack propagation necessitates sufficient strain energy to surpass the energy required for material surface formation [32]. The formation of cracks results in the creation of two intergranular crack surfaces. Enhancing the crack area through meandering can effectively impede crack propagation. At temperatures below the DBTT, pure W exhibits minimal plastic deformability, indicating that brittle fracture predominates as the primary failure mode in this scenario. When brittle fracture occurs, the occurrence of either intergranular or transgranular fracture is influenced by various factors, including grain size and shape. However, the impurity levels at the grain boundary play an increasingly significant role [33].

Intergranular fracture predominates as the primary mode of failure in PBF–LB pure tungsten, indicating a reduced strength at grain boundaries and emphasizing their critical role in crack initiation. Braun et al. [34] reported that oxygen is segregated as tungsten oxide at grain boundaries during PBF–LB W processing, leading to the formation of hot or cold cracks. This observation highlights the significant reduction in grain boundary strength caused by impurity segregation. In the PBF–LB W samples, a variety of defects can be observed in the microstructure, including intergranular TCs, ECs, NECs and aggregated nanopores (Fig. 8). The aggregation of nanopores is evident along grain boundaries in single tracks, thin walls, and cubes. Scholars have previously reported the presence of nanopores in the PBF–LB W microstructure and identified them as potential sources of crack initiation [11,35]. The generation of nanopores in previous studies has been attributed to the boiling of W oxides [36] or trapped Ar gas [23,35]. However, the appearance and aggregation of nanopores during the PBF–LB W process have proven to be inevitable thus far. Based on the stress concentration, it can be inferred that the aggregation of nanopores along grain boundaries can weaken the strengths of these boundaries in W.

Moreover, it can be reasonably inferred that a decrease in nanopore size and an increase in nanopore spacing results in a reduced cracking threshold. Interestingly, the presence of nanopore footprints is observed around certain ECs (Fig. 8(f)) and NECs (Fig. 8(d)), while microcracks consisting of aggregated nanopores have been documented in previous studies [11,23]. Therefore, it is reasonable to observe that the aggregation of nanopores can weaken grain boundary strength and facilitate crack formation. The weakening effect of nanopore aggregation can be evaluated using a fracture mechanical model (Supplementary Information). This model considers the influences of the nanopore radius ρ and the center spacing d between adjacent nanopores on the critical strength. A higher value of the size factor $2\rho/d$ corresponds to a lower crack threshold.

By considering the typical values of ρ and d as 25 nm and 100 nm, respectively, in Fig. 8(c_2), supplementary calculations demonstrate that the aggregation of nanopores at GBs can significantly weaken their strength by approximately 70 %, thereby rendering W increasingly susceptible to cracking due to its intrinsic brittleness.

Based on postmortem observations and previous studies [11,20,23], we propose a three-stage mechanism (Fig. 14) to explain the influences of nanopores on the weaknesses of GBs and crack formation in PBF–LB pure tungsten:

During the PBF–LB process, W powder is laser-scanned, melted, solidified, and subsequently cooled to match the substrate temperature. In this procedure, nanopores tend to aggregate at GBs, forming weak links that can further evolve into ECs and NECs. In Stage I, nanopores are generated at high temperatures (close to/reach the melting point). The strings of nanopores are aligned along GBs. The nanopores along GBs at elevated temperatures have the potential to diffuse and rearrange during the cooling process. In Stage II, two scenarios can occur based on the nanopore radius ρ and center spacing d. If the size factor $2\rho/d$ is relatively small, upon further cooling below DBTT, the string of nanopores will be retained (phenomenon I). Conversely, if the size factor $2\rho/d$ is relatively large, the nanopores will coalesce into microcracks. Under further cooling (Stage III), if the strain energy surpasses the threshold required for the formation of two fracture surfaces, the interconnected nanopores will propagate into extended cracks (phenomenon III); otherwise, the interconnected nanopores will persist as nonextended cracks (phenomenon II).

In addition to the interconnected nanopores, if impurity segregation is incorporated during manufacturing, the impact on grain boundary strength will be exacerbated. The critical size factor and corresponding fracture stress will be significantly reduced as a result. Therefore, efforts to minimize nanopores and impurities are imperative for mitigating crack formation in PBF–LB W.

4.2. Formation analysis of longitudinal cracks in PBF–LB W single tracks

The significance of studying single tracks lies in their role as fundamental components of PBF–LB cubes, where the microstructure and crack behavior observed in single melt tracks are inherited. Vrancken et al. [20] have previously reported that longitudinal cracking tends to occur at high laser powers, resulting in wide and deep molten pools, which is consistent with the findings presented in Fig. 5 of the single track study. It is worth noting that the occurrence of a longitudinal crack at the fusion zone midline in the single melt track can be attributed to the periodic temperature field, which consequently leads to the generation of periodic thermal cycles in the PBF–LB W cube.

To gain further insights into the cause of longitudinal cracking in the middle of the FZ during PBF–LB single tracks, finite element (FE) calculations can be conducted to analyze the temperature and stress distribution characteristics within the FZ during and after laser irradiation. Supplementary details are provided for reference. The FE simulation reveals a significant concentration of stress near the center of the FZ, with a maximum stress exceeding 800 MPa. Additionally, the solidification process depicted in Fig. 5 may result in a preference for high-angle grain boundaries (HAGBs) as potential crack paths within the fusion zone center. Altogether, these findings offer a plausible explanation for the occurrence of longitudinal cracks at this specific location, where an abundance of densely distributed HAGBs leads to stress concentration.

In the single track experiment, an increase in laser energy input results in an increase in the fusion zone depth and the induction of longitudinal cracks. This observation implies a correlation between the depth of the fusion zone and the occurrence of longitudinal cracks. By analyzing the energy framework, it is evident that a long longitudinal crack formed within a deep fusion zone can release additional strain energy. Therefore, it is suggested that the formation of longitudinal cracks may be facilitated by deep fusion zones. The observed correlation between the depth of the fusion zone and the occurrence of longitudinal crack formation aligns with previous findings reported by Vrancken [20] and Higashi [37].

Based on the analysis of thermal stress and grain boundary weakness, a comparative investigation can be conducted to analyze cracking in PBF–LB W single tracks and cubes. The single track demonstrates a lower

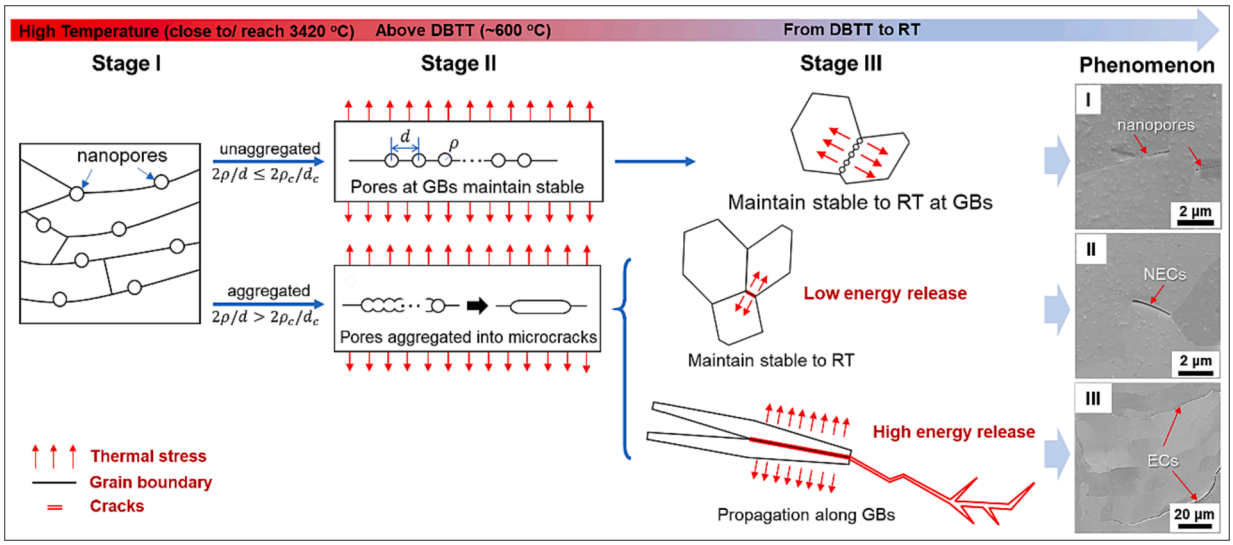

Fig. 14. Schematic illustration of the cracking mechanism based on nanopores in PBF–LB W. (Stage I) Nanopore formation. (Stage II) Nanopore rearrangement and aggregation phenomenon above DBTT. (Stage III) Behaviors of nanopores and microcracks below DBTT.

cracking threshold than the cubic sample under the same laser parameters. This phenomenon can be comprehended by considering the influences of both microstructures and thermal stresses.

The comparison of grain structures between the FZ center in a single track and one of the melt tracks in the cube is illustrated in Fig. 15. The adjacent grain structures to the FZ center are extracted for analysis. The results reveal that the grain morphology within the FZ center of a single track exhibits equiaxed characteristics, while the boundaries at the centerline of the molten pool appear highly tortuous (Fig. 15(a_1)).

In contrast, the epitaxial growth of grains in the PBF–LB cube process

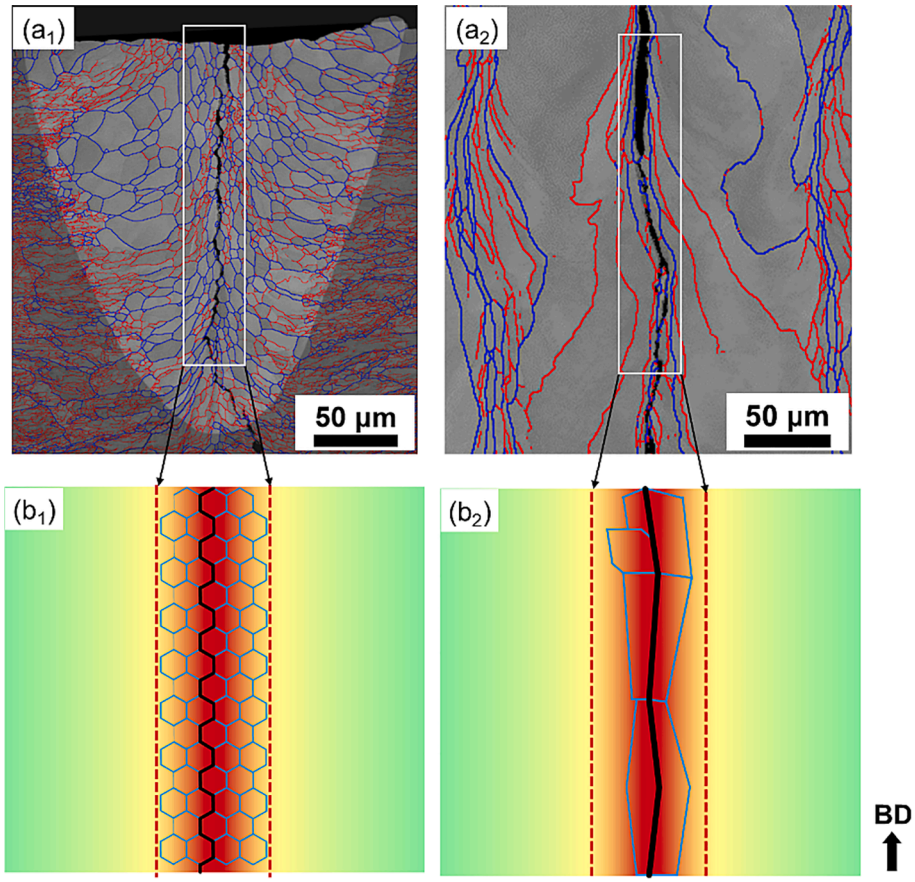

Fig. 15. Comparison of grain structures (a_1, b_1) in the FZ center in a single track and (a_2, b_2) in one of the melt tracks in the cube under the same stress contribution. (a_1, a_2) EBSD quality images superimposed HAGBs by blue lines and low-angle grain boundaries (LAGBs) by red lines, showing the grain morphologies in the FZ center. (b_1, b_2) Schematic diagram of the grain morphology and the stress distribution extracted from (a_1, a_2), marked with white rectangles. Red is indicative of high levels of stress, while green signifies low levels of stress.

results in pronounced high-angle grain boundaries at the FZ center, exhibiting a relatively flat morphology (Fig. 15(a_2)). The stress simulation above reveals the presence of stress concentration during single-track deposition. It is suggested that the melt tracks exhibit similar temperature and stress fields during bulk deposition, albeit with minor asymmetry [38]. Additionally, strain accumulation is expected to occur. Therefore, it is suggested that straight HAGBs located at the center of the FZ within the stress-concentrated region are highly conducive to crack propagation. Additionally, this analysis indicates that the presence or absence of cracks in the preprinted substrate has minimal influence on crack generation during subsequent bulk forming processes.

4.3. Deformation-cracking competition in PBF–LB W

According to the analysis of longitudinal, horizontal, and transverse planes in Section 3.2, we reveal the arrangements of through cracks and the structures of grains. In the longitudinal planes, cracks are arranged at every single hatch in unidirectional samples, while they are arranged at every other hatch in bidirectional samples. Overall, the findings in longitudinal planes are aligned with those obtained from horizontal planes.

To investigate the correlation between intergranular cracking and microstructure, Fig. 16 displays the densities of HAGBs and LAGBs in longitudinal planes using two scanning strategies extracted from Fig. 7. The boundary density is calculated by counting misorientation within a distance step of 50 μm across nine molten pools. The boundary density is calculated by multiplying the number of pixels with the corresponding step size for the misorientation angle range. In this context, the boundary density proves to be a more reliable microstructural characteristic than grain size.

The grain boundary distribution images (Fig. 16(b_1, b_2)) clearly reveal that the boundaries, including HAGBs and LAGBs, are predominantly concentrated in the middle region of the FZ. Conversely, a significant decrease in boundary density is observed at other locations within the molten pools. In a unidirectional microstructure, these boundaries form a periodic ladder-like microstructure composed of curved grains, whereas in a bidirectional microstructure, the boundaries tend to be inclined along the building direction.

The middle zone and gap zone in Fig. 16(c) are defined as the regions with a half hatch spacing step, i.e., 50 μm, that surround and deviate from the centerline of the FZ, respectively. The boundary densities in the microstructure exhibit distinct periodic fluctuations corresponding to the division between these two zones. The boundary density of the middle zone in Fig. 16(b_1, b_2) is approximately 2 to 3 times higher than that of the gap zone for each scanning strategy employed. This observation not only suggests that the middle zone experiences greater deformation and stress concentration during the PBF–LB process but also indicates its role as a junction for epitaxial growth grains, thereby contributing to the formation of a fine microstructure.

In summary, the grain boundary strength in PBF–LB pure W is primarily deteriorated by three factors: (i) the presence of high-angle and elongated straight grain boundaries with elevated interface energy, rendering them highly susceptible to crack propagation; (ii) impurity segregation along grain boundaries; and (iii) stress concentration resulting from nanopore aggregation along grain boundaries. Moreover, the primary external and internal reasons for cracking in PBF–LB W are attributed to thermal strain and low grain boundary strength, respectively [10,20]. In the unidirectional sample, each melt track is considered an individual periodic scanning track. The former melt track has completely solidified during the overlap with the adjacent one. In the bidirectional sample, there is no apparent cracking at every single hatch. One possible explanation is that the materials can effectively distribute strain through displacement to alleviate stress after the formation of through cracks, thereby reducing constraints on adjacent melt tracks. The occurrence of cracks serves as a crucial mechanism for releasing strain energy. As mentioned in Section 4.1, cracks develop when the thermal strain surpasses the energy required for generating fracture surfaces. However, from an energy perspective, the release of strain energy can occur through alternative mechanisms, such as storage within materials via deformation and transformation into stored energy as dislocations and LAGBs. Nevertheless, due to the limited deformability of W at low temperatures, mitigating cracking remains challenging when subjected to extreme thermal stress during PBF–LB processes.

According to the analysis of grain boundaries and crack morphologies, the microstructure–crack relationship can be established in the two parallel-hatching scanned samples. During the PBF–LB W process, a portion of the strain energy is stored within the materials as LAGBs or

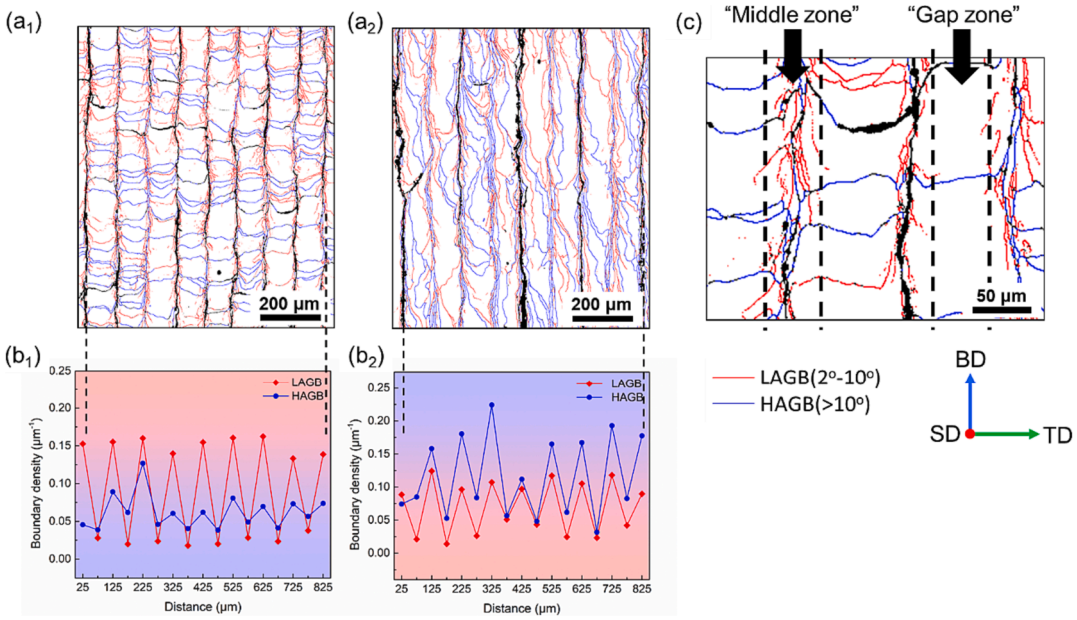

Fig. 16. Densities of the grain boundaries in longitudinal planes with (a_1, b_1) unidirectional and (a_2, b_2) bidirectional scanning strategies with a distance step of 50 μm. (a_1, a_2) EBSD maps with a 0.5 μm scanning step are superimposed HAGBs by blue lines and LAGBs by red lines. (c) Locations of the middle zone and gap zone, visually classified by the black dashed lines.

boundaries with an angular deviation less than 2°, while another portion is released through cracking. Based on the preceding discussion, we propose a deformation-cracking competition mechanism in PBF–LB W. The generation of low-angle grain boundaries and cracking along HAGBs represent two potential avenues for relieving thermal stress. When thermal stress becomes concentrated within the middle region of the FZ, both deformation and cracking are likely to occur. The formation of cracks is determined not only by the deformability of materials but also by the strengths of grain boundaries. Specifically, thermal stress induces both elastic and plastic deformation in the W matrix during the PBF–LB process. The occurrence of LAGBs can be primarily attributed to plastic deformation. Once the thermal stress released by deformation is higher than the grain boundary strength, rapid propagation of cracking along high-angle grain boundaries occurs. Given the limited ability of W to undergo plastic deformation at room temperature, the cracking threshold of pure W is primarily determined by its grain boundary strength. In the PBF–LB pure W study reported by Brun et al. [34], a significant presence of oxides is observed on the intergranular fracture surfaces of bulks prepared using powders containing an oxygen content of 800 ppm. The XRF measurements conducted in this study indicate an oxygen content of 580 ppm for the PBF–LB W cubes, suggesting potential weakening of grain boundary strength due to oxygen. Therefore, to mitigate the cracking of PBF–LB W, it is imperative to (i) enhance the presence of low-angle and short zigzag grain boundaries with relatively low interfacial energies, (ii) suppress the segregation of impurities (e.g., O, Ar) along GBs, and (iii) regulate the aggregation of nanopores in the grains. These three influencing factors are crucial for enhancing the strengths of grain boundaries. Additionally, conducting the PBF–LB process at an elevated ambient temperature can significantly enhance the deformability of W and serve as a crucial measure for mitigating thermal stress.

4.4. Geometric effects on the cracks and microstructures in PBF–LB W thin walls

The influence of geometry on the temperature field during the PBF–LB process has been widely acknowledged, including the height effect [39] and geometric effect [40,41]. The geometric effect can be investigated through the multiwall experiment. In the thin wall experiment shown in Fig. 13, through cracks are observed in walls with more than three tracks, while no through cracks are formed in walls with one or two tracks. The grain sizes in the thin walls with more than three tracks are consistent with those of the base plate, while they are slightly larger than those in the thin walls with one or two tracks. This observation indicates the presence of a threshold for through crack formation corresponding to different wall thicknesses, which can be attributed to the relationship between constraints and thermal stress. Thin walls with one or two melt tracks exhibit a reduced transverse constraint, decreasing the thermal stress. As the wall thickness increases, the contact area between the multiwall and printed base plate expands, leading to increased heat dissipation and thermal stress levels. The ladder-like shape and grain size characteristics of the solidification grains in thin walls with more than three tracks resemble those of the base plate, suggesting that they undergo similar thermal and strain fields.

The simulation study conducted by Parry et al. [40] examined the impacts of geometry on thermal history and residual stress distribution, providing valuable insights that align well with our experimental findings for thin wall samples. Specifically, this investigation of rectangular geometry reveals significant transverse stress values in the central region, which rapidly decrease toward the outer edges. Our results demonstrate that thin walls containing one or two melt tracks do not exhibit the presence of TCs, whereas thin walls with more than three melt tracks consistently exhibit the occurrence of TCs, aligning with the simulation results of Parry et al.

A plausible formation process of thin walls in TCs is elucidated as follows: During PBF–LB W thin wall printing, the overlap between molten pools results in a rigid constraint after solidification. The primary stress influencing TC formation is expected to be thermal stress along the transverse direction. The presence of more than three melt tracks in the thin walls indicates that the periodic scanning strategy in PBF–LB W cubes commonly leads to the formation of TCs, owing to significant temperature gradients imposed by constraints in both positive and negative transverse directions.

In summary, the multiwall experiment of PBF–LB W demonstrates the influences of geometry on the thermal field, microstructure, and crack behavior.

4.5. Implications and recommendations

In previous studies on additive manufactured (AM) W, although localized regions with minimal crack occurrence have been observed, achieving crack elimination across all regions remains a challenging task, which constitutes the fundamental issue in addressing microstructural cracks. Notably, only a limited number of references provide information on the tensile strength of low-alloyed W alloys in recent research on additive manufacturing of tungsten [42]. The results obtained from additive manufacturing are significantly lower than those achieved through traditional manufacturing, primarily due to the presence of numerous cracks in the matrix. Consequently, it is feasible to identify noncracked regions within samples containing cracks. In this study, crack location-controlled microstructures are successfully generated using parallel-hatching scanning strategies. For future investigations on suppressing cracks in PBF–LB, we recommend conducting comparative experiments, such as experiments on printed cracked base-plate samples.

The PBF–LB technology exhibits the characteristics of scanning track-by-track and layer-by-layer, resulting in a periodic microstructure that mirrors the periodicity of the manufacturing process. In this study, an exceptional advantage of employing parallel-hatching scanning strategies is the ability to achieve crack location-controlled microstructures by precisely controlling the periodicity of the PBF–LB process.

Specifically, based on a comprehensive understanding of the periodic scanning characteristics inherent to PBF–LB, we conduct region divisions and boundary density analysis instead of focusing solely on grain sizes. It is important to note that different angles of the boundaries correspond to distinct solidification and deformation processes. By employing these manufacturing strategies, microstructures within various fusion zone regions can be effectively classified and discussed relative to their cracking behavior.

The present study systematically elucidates the cracking behavior of PBF–LB W through a series of experiments, ranging from single tracks and thin walls to cubes and pseudo-3D reconstructions. Specifically, the diverse sample geometries investigated in this study offer a comprehensive perspective on the crack formation mechanism in PBF–LB W. It is widely recognized that PBF–LB, as an immensely versatile additive manufacturing process capable of producing intricate and customized structures, holds significant industrial significance.

Furthermore, our findings demonstrate the scientific significance of this adaptability by facilitating the design of tailored specimens to support fundamental research. For instance, we successfully integrate various thicknesses of thin walls into a single sample, thereby reducing the time required for sample polishing and enabling an in-depth exploration of the size effects in PBF–LB. Additionally, the utilization of a geometric approach in this study, as observed in previous research [41,43–45], allows for the examination of microstructure evolution and highlights the additive nature of PBF–LB. Bertsch et al. [43] further expanded on this concept by employing various sample geometries, such as 1D rods, 2D walls, and 3D prisms, to investigate dislocation structures in AM 316L. We recommend the investigation of AM-related phenomena for samples with meticulously designed geometries.

In future research, we propose three directional solutions to mitigate the occurrence of cracks in additively manufactured pure W

components. First, the grain boundary strength should be improved. Improving the resistance of the cracking propagation of W by refining grains, such as heterogeneous nucleation, constitutional supercooling, reducing nanopores, reducing impurity segregation at grain boundaries (such as adding oxygen absorbing components) and controlling the powder oxygen and chamber atmosphere. Second, thermal stress should be reduced during the process, such as substrate preheating, to alleviate the temperature gradient and cooling rate. Although preheating a substrate at 1000 ℃ can partially mitigate cracks in W parts, it is challenging to achieve this treatment to date, especially in engineering. Alternatively, in situ annealing has been proposed as an effective method for significantly reducing thermal stress [46]. Additionally, modifying the laser spot size [47] and employing spot oscillation technology [48] have both demonstrated potential in minimizing thermal stress. Third, matrix deformability should be improved, such as through low alloying and substrate preheating (above DBTT), to enhance the capability of dislocation motion.

5. Conclusions

In this study, the crack behaviors of single tracks, thin walls, and cubes in PBF–LB pure W were systematically investigated in nonrotational parallel-hatching scanning strategies, revealing valuable insights into the underlying mechanisms. A comprehensive understanding of the periodic cracking arrangement in PBF–LB W was established, elucidating the relationships among scanning paths, solidification microstructures, and cracking behaviors. The value of strain energy was crucial for the propagation of cracks, as it had to overcome the energy required to create two surfaces. This energy framework was employed to elucidate the underlying mechanism of crack formation. Strategies aimed at mitigating cracking in W through additive manufacturing were presented. The findings could be summarized as follows:

(1) Concerning grain boundary strength, by comparing the microstructures around central cracks of single tracks and cubes, the straight HAGBs at the stress concentrated area in the FZ center are found to be conducive to crack propagation. The weakening effect of nanopores on grain boundary strength in PBF–LB W is approximately 70 %. Additionally, the presence of oxygen has a potential weakening effect on grain boundary strength. Therefore, enhancing the strengths of grain boundaries necessitates improvements in three key factors: boundary morphologies, impurity levels, and nanopores.
(2) Regarding the thermal stress during the PBF–LB process, the multiwall experiment reveals the geometric effect, indicating that there is a threshold for the formation of TCs corresponding to different wall thicknesses. As the melt tracks decrease in the multiwall structure, the constraint along the TD is reduced. Consequently, during cooling, small thermal stresses are generated, which provides an advantage in suppressing crack formation.
(3) According to the analyses of grain boundaries and crack morphologies in the two parallel-hatching scanned cubes, a deformation-cracking competition mechanism in PBF–LB W is proposed. The generation of low-angle grain boundaries and cracking along HAGBs represent two potential avenues for relieving thermal stress. The formation of cracks is determined by material deformability and grain boundary strength.

In future studies, three directional solutions are proposed to mitigate the occurrence of cracks in additively manufactured pure W:

- The grain boundary strength should be improved. Specific ways such as improving the resistance of the cracking propagation of W through grain refinement, such as through heterogeneous nucleation and constitutional supercooling; reducing nanopores; reducing impurity segregation at grain boundaries, such as by adding oxygen absorbing components; and controlling the powder oxygen and the PBF–LB chamber atmosphere.
- Thermal stress should be reduced during the process, such as by substrate preheating.
- The matrix deformability should be improved, such as low alloying and substrate preheating (above DBTT), to enhance the capability of dislocation motion.

Declaration of Competing Interest

The authors declare that they have no known competing financial interests or personal relationships that could have appeared to influence the work reported in this paper.

Data availability

Data will be made available on request.

Acknowledgements

The authors acknowledge the financial support of the National Magnetic Confinement Fusion Science Program of China [Grant number 2019YFE03130003, 2022YEF03130003]; and the National Natural Science Foundation of China [Grant number 51971115, 52001135, 52105165, 52275391]; and China Postdoctoral Science Foundation [Grant number 2022M711753]. The authors would like to thank School of Aerospace Engineering, Tsinghua University for supporting the research. Besides, the authors would like to thank the mentor Professor Shen James Zhijian, who has passed away, for his guidance and help. We will continue to move forward under the guidance of his spirit in future study and work.

Appendix A. Supplementary data

Supplementary data to this article can be found online at https://doi.org/10.1016/j.matdes.2023.112363.

References

[1] D.Z. Wang, K.L. Li, C.F. Yu, J. Ma, W. Liu, Z.J. Shen, Cracking behavior in additively manufactured pure tungsten, Acta Metallurgica Sinica (english Letters) 32 (1) (2018) 127–135.
[2] A.T. Sidambe, Y. Tian, P.B. Prangnell, P. Fox, Effect of processing parameters on the densification, microstructure and crystallographic texture during the laser powder bed fusion of pure tungsten, Int. J. Refract Metal Hard Mater. 78 (1) (2019) 254–263.
[3] G. Pintsuk, Tungsten as a Plasma-Facing Material, Comprehensive Nucl. Mater. (2012) 551–581.
[4] V. Philipps, Tungsten as material for plasma-facing components in fusion devices, J. Nucl. Mater. 415 (1) (2011) S2–S9.
[5] S. Wurster, N. Baluc, M. Battabyal, T. Crosby, Recent progress in R&D on tungsten alloys for divertor structural and plasma facing materials, J. Nucl. Mater. 442 (1–3) (2013) S181–S189.
[6] B.G. Butler, J.D. Paramore, J.P. Ligda, C. Ren, Z.Z. Fang, S.C. Middlemas, K. J. Hemker, Mechanisms of deformation and ductility in tungsten - A review, Int. J. Refract Metal Hard Mater. 75 (2018) 248–261.
[7] A.V. Müller, G. Schlick, R. Neu, C. Anstätt, T. Klimkait, J. Lee, B. Pascher, M. Schmitt, C. Seidel, Additive manufacturing of pure tungsten by means of selective laser beam melting with substrate preheating temperatures up to 1000 ◦C, Nuclear Materials and Energy 19 (2019) 184–188.
[8] A. Iveković, N. Omidvari, B. Vrancken, K. Lietaert, L. Thijs, K. Vanmeensel, J. Vleugels, J.-P. Kruth, Selective laser melting of tungsten and tungsten alloys, Int. J. Refract Metal Hard Mater. 72 (2018) 27–32.
[9] A.C. Field, L.N. Carter, N.J.E. Adkins, M.M. Attallah, et al., The effect of powder characteristics on build quality of high-purity tungsten produced via laser powder bed fusion (PBF-LB), Metall. Mater. Trans. A 51 (3) (2020) 1367–1378.
[10] K. Li, D. Wang, L. Xing, Y. Wang, C. Yu, J. Chen, T. Zhang, J. Ma, W. Liu, Z. Shen, Crack suppression in additively manufactured tungsten by introducing secondary-phase nanoparticles into the matrix, Int. J. Refract Metal Hard Mater. 79 (1) (2019) 158–163.
[11] D. Wang, Z. Wang, K. Li, J. Ma, W. Liu, Z. Shen, Cracking in laser additively manufactured W: Initiation mechanism and a suppression approach by alloying, Mater. Des. 162 (1) (2019) 384–393.

[12] K. Li, G. Ma, L. Xing, Y. Wang, C. Yu, J. Chen, J. Ma, G. Wu, W. Liu, Z. Shen, X. Huang, Crack suppression via in-situ oxidation in additively manufactured W-Ta alloy, Mater. Lett. 263 (2020) 127212.
[13] C. Tan, K. Zhou, W. Ma, B. Attard, et al., Selective laser melting of high-performance pure tungsten: parameter design, densification behavior and mechanical properties, Sci. Technol. Adv. Mater. 19 (1) (2018) 370–380.
[14] R.K. Enneti, R. Morgan, S.V. Atre, Effect of process parameters on the Selective Laser Melting (SLM) of tungsten, Int. J. Refract Metal Hard Mater. 71 (2018) 315–319.
[15] Z. Xiong, P. Zhang, C. Tan, D. Dong, W. Ma, K. Yu, Selective laser melting and remelting of pure tungsten, Adv. Eng. Mater. 22 (1901352) (2020) 1–9.
[16] V. D, Residual Stress Evaluation by the Hole-Drilling Method With Off-Center Hole_ An Extension of the Integral Method, J. Eng. Mater. Technol. 119 (1997) 7.
[17] P. Pagliaro, M.B. Prime, H. Swenson, B. Zuccarello, Measuring multiple residual-stress components using the contour method and multiple cuts, Exp. Mech. 50 (2) (2010) 187–194.
[18] A.J. Allen, M.T. Hutchings, C.G. Windsor, C. Andreani, Neutron diffraction methods for the study of residual stress fields, Adv. Phys. 34 (4) (2006) 445–473.
[19] A. Müller, G. Schlick, R. Neu, C. Anstätt, et al., Additive manufacturing of pure tungsten by means of selective laser beam melting with substrate preheating temperatures up to 1000 °C, Nuclear Mater. Energy 19 (1) (2019) 184–188.
[20] B. Vrancken, R.K. Ganeriwala, M.J. Matthews, Analysis of laser-induced microcracking in tungsten under additive manufacturing conditions: experiment and simulation, Acta Mater. 194 (1) (2020) 464–472.
[21] M. Guo, D. Gu, L. Xi, H. Zhang, et al., Selective laser melting additive manufacturing of pure tungsten: Role of volumetric energy density on densification, microstructure and mechanical properties, Int. J. Refract Metal Hard Mater. 84 (105025) (2019) 1–11.
[22] S. Wen, C. Wang, Y. Zhou, L. Duan, W. Wei, S. Yang, Y. Shi, High-density tungsten fabricated by selective laser melting: Densification, microstructure, mechanical and thermal performance, Opt. Laser Technol. 116 (1) (2019) 128–138.
[23] T. Yamamoto, M. Hara, Y. Hatano, Effects of fabrication conditions on the microstructure, pore characteristics and gas retention of pure tungsten prepared by laser powder bed fusion, Int. J. Refract Metal Hard Mater. 95 (105410) (2021) 1–9.
[24] W. Yu, S.L. Sing, C.K. Chua, X. Tian, Influence of re-melting on surface roughness and porosity of AlSi10Mg parts fabricated by selective laser melting, J. Alloy. Compd. 792 (1) (2019) 574–581.
[25] Lowrie R, Gonas A M, Single-crystal elastic properties of tungsten from 24° to 1800 °C, J. Appl. Phys. 38(11) (1967) 4505-4509.
[26] E. Lassner, W.D. Schubert, Tungsten properties, chemistry, technology of the element, alloys, and chemical compounds, Springer Science & Business Media, 1999.
[27] C. Luo, J. Qiu, Y. Yan, J. Yang, C. Uher, X. Tang, Finite element analysis of temperature and stress fields during the selective laser melting process of thermoelectric SnTe, J. Mater. Process. Technol. 261 (2018) 74–85.
[28] Y. Liu, J. Zhang, Z. Pang, Numerical and experimental investigation into the subsequent thermal cycling during selective laser melting of multi-layer 316L stainless steel, Opt. Laser Technol. 98 (1) (2018) 23–42.
[29] H.L. Wei, J.W. Elmer, T. DebRoy, Crystal growth during keyhole mode laser welding, Acta Mater. 133 (1) (2017) 10–20.
[30] T.I. Tsubasa Todo, O. Gokcekaya, O.h. Jongyeong, Takayoshi Nakano, Single crystalline-like crystallographic texture formation of pure tungsten through laser powder bed fusion, Scr. Mater. 206 (2022), 114252.
[31] Kruth J P, Deckers J, Yasa E, Wauthlé R, Assessing and comparing influencing factors of residual stresses in selective laser melting using a novel analysis method, Proceedings of the institution of mechanical engineers, Part B: J. Eng. Manuf. 226 (6) (2012) 980-991.
[32] T.L. Anderson, Fracture mechanics: fundamentals and applications, CRC Press, 2017.
[33] B. Gludovatz, Fracture behavior of tungsten, Austrian Academy of Sciences, University of Leoben, 2010.
[34] J. Braun, L. Kaserer, J. Stajkovic, K.H. Leitz, et al., Molybdenum and tungsten manufactured by selective laser melting: Analysis of defect structure and solidification mechanisms, Int. J. Refract Metal Hard Mater. 84 (104999) (2019) 1–9.
[35] T. Yamamoto, M. Hara, Y. Hatano, Cracking behavior and microstructural, mechanical and thermal characteristics of tungsten–rhenium binary alloys fabricated by laser powder bed fusion, Int. J. Refract Metal Hard Mater. 100 (105651) (2021) 1–12.
[36] D. Wang, Z. Wang, K. Li, J. Ma, W. Liu, Z. Shen, Cracking in laser additively manufactured W: Initiation mechanism and a suppression approach by alloying, Mater. Des. 162 (2019) 384–393.
[37] M. Higashi, T. Ozaki, Selective laser melting of pure molybdenum: Evolution of defect and crystallographic texture with process parameters, Mater. Des. 191 (108588) (2020) 1–11.
[38] L. Parry, I.A. Ashcroft, R.D. Wildman, Understanding the effect of laser scan strategy on residual stress in selective laser melting through thermo-mechanical simulation, Addit. Manuf. 12 (1) (2016) 1–15.
[39] T.R. Smith, J.D. Sugar, C. San Marchi, J.M. Schoenung, Strengthening mechanisms in directed energy deposited austenitic stainless steel, Acta Mater. 164 (1) (2019) 728–740.
[40] L.A. Parry, I.A. Ashcroft, R.D. Wildman, Geometrical effects on residual stress in selective laser melting, Addit. Manuf. 25 (1) (2019) 166–175.
[41] X. Wang, J.A. Muniz-Lerma, O. Sánchez-Mata, M. Attarian Shandiz, M. Brochu, Microstructure and mechanical properties of stainless steel 316L vertical struts manufactured by laser powder bed fusion process, Mater. Sci. Eng. A 736 (1) (2018) 27–40.
[42] C.C. Eckley, R.A. Kemnitz, C.P. Fassio, C.R. Hartsfield, T.A. Leonhardt, Selective Laser Melting of Tungsten-Rhenium Alloys, JOM 73 (11) (2021) 3439–3450.
[43] K.M. Bertsch, G. Meric de Bellefon, B. Kuehl, D.J. Thoma, Meric de Bellefon G, Kuehl B, Thoma D J, Origin of dislocation structures in an additively manufactured austenitic stainless steel 316L, Acta Mater. 199 (2020) 19–33.
[44] A.D. Dressler, E.W. Jost, J.C. Miers, D.G. Moore, C.C. Seepersad, B.L. Boyce, Heterogeneities dominate mechanical performance of additively manufactured metal lattice struts, Addit. Manuf. 28 (2019) 692–703.
[45] A. Banerjee, S. Messina, M.R. Begley, E.J. Schwalbach, M.A. Groeber, W. D. Musinski, P.A. Shade, M.E. Cox, J.D. Miller, K.J. Hemker, The mechanical response of additively manufactured IN625 thin-walled structures, Scr. Mater. 205 (2021) 114188.
[46] W.L. Smith, J.D. Roehling, M. Strantza, R.K. Ganeriwala, A.S. Ashby, B. Vrancken, B. Clausen, G.M. Guss, D.W. Brown, J.T. McKeown, M.R. Hill, M.J. Matthews, Residual stress analysis of in situ surface layer heating effects on laser powder bed fusion of 316L stainless steel, Addit. Manuf. 47 (2021) 102252.
[47] A. Iveković, M.L. Montero-Sistiaga, J. Vleugels, J.P. Kruth, et al., Crack mitigation in Laser Powder Bed Fusion processed Hastelloy X using a combined numerical-experimental approach, J. Alloy. Compd. 864 (158803) (2021) 1–11.
[48] J.P. Oliveira, T.G. Santos, R.M. Miranda, Revisiting fundamental welding concepts to improve additive manufacturing: from theory to practice, Prog. Mater Sci. 107 (100590) (2020) 1–43.